Detection, visualization and animation of abnormal anatomic structure with a deformable probabilistic brain atlas based on random vector field transformations

Paul M. Thompson and Arthur W. Toga*

Laboratory of Neuro Imaging, Department of Neurology, Division of Brain Mapping, UCLA School of Medicine, Los Angeles, CA 90095-1769, USA

Abstract

This paper describes the design, implementation and preliminary results of a technique for creating a comprehensive probabilistic atlas of the human brain based on high-dimensional vector field transformations. The goal of the atlas is to detect and quantify distributed patterns of deviation from normal anatomy, in a 3-D brain image from any given subject. The algorithm analyzes a reference population of normal scans and automatically generates color-coded probability maps of the anatomy of new subjects. Given a 3-D brain image of a new subject, the algorithm calculates a set of high-dimensional volumetric maps (with typically $384^2 \times 256 \times 3 \approx 10^8$ degrees of freedom) elastically deforming this scan into structural correspondence with other scans, selected one by one from an anatomic image database. The family of volumetric warps thus constructed encodes statistical properties and directional biases of local anatomical variation throughout the architecture of the brain. A probability space of random transformations, based on the theory of anisotropic Gaussian random fields, is then developed to reflect the observed variability in stereotaxic space of the points whose correspondences are found by the warping algorithm. A complete system of $384^2 \times 256$ probability density functions is computed, yielding confidence limits in stereotaxic space for the location of every point represented in the 3-D image lattice of the new subject's brain. Color-coded probability maps are generated, densely defined throughout the anatomy of the new subject. These indicate locally the probability of each anatomic point being unusually situated, given the distributions of corresponding points in the scans of normal subjects. 3-D MRI and high-resolution cryosection volumes are analyzed from subjects with metastatic tumors and Alzheimer's disease. Gradual variations and continuous deformations of the underlying anatomy are simulated and their dynamic effects on regional probability maps are animated in video format (on the accompanying CD-ROM). Applications of the deformable probabilistic atlas include the transfer of multi-subject 3-D functional, vascular and histologic maps onto a single anatomic template, the mapping of 3-D atlases onto the scans of new subjects, and the rapid detection, quantification and mapping of local shape changes in 3-D medical images in disease and during normal or abnormal growth and development.

Keywords: 3-D stereotaxic space, brain mapping, morphometry, non-linear image registration, probabilistic atlas

1. INTRODUCTION

Remarkable variations exist, across individuals, in the internal and external geometry of the brain. In the past, comparing data from different subjects or patient subpopulations has been difficult because cortical topography and the internal geometry of the brain vary so greatly (Ono *et al.*, 1990). At the same time, much research has been directed towards the development of standardized three-dimensional atlases of the

*Corresponding author
(e-mail: toga@loni.ucla.edu)

human brain (Talairach and Tournoux, 1988; Greitz *et al.*, 1991; Höhne *et al.*, 1992; Thurfjell *et al.*, 1993; Kikinis *et al.*, 1996). These provide an invariant reference system and the possibility of template matching, allowing anatomical structures in new scans to be identified and analyzed. Atlases serve as a guide in planning stereotaxic neurosurgical procedures and provide a precise quantitative framework for multi-modality brain mapping.

1.1. Deformable and probabilistic brain atlases

1.1.1. Deformable atlases

In view of the complex structural variability between individuals, a fixed brain atlas may fail to serve as a faithful representation of every brain (Roland and Zilles, 1994; Mazziotta *et al.*, 1995). It would, however, be ideal if the atlas could be elastically deformed to fit a new image set from an incoming subject. Transforming individual datasets into the shape of a single reference anatomy, or onto a 3-D digital brain atlas, removes subject-specific shape variations and allows subsequent comparison of brain function between individuals (Christensen *et al.*, 1993). Conversely, high-dimensional warping algorithms (Christensen *et al.*, 1993, 1996; Collins *et al.*, 1994a; Rabbitt *et al.*, 1995; Thirion, 1995; Davatzikos, 1996; Thompson and Toga, 1996a, Bro-Nielsen and Gramkow, 1996) can also be used to transfer all the information in a 3-D digital brain atlas onto the scan of any given subject, while respecting the intricate patterns of structural variation in their anatomy. Such deformable atlases (Evans *et al.*, 1991; Christensen *et al.*, 1993; Gee *et al.*, 1993; Sandor and Leahy, 1994, 1995) can be used to carry 3-D maps of functional and vascular territories into the coordinate system of different patients, as well as information on different tissue types and the boundaries of cytoarchitectonic fields and their neurochemical composition. Thirdly, 3-D warping algorithms, such as the one featured in our video which accompanies this paper, provide a method for calculating local and global shape changes and produce valuable information about normal and abnormal growth and development (Toga *et al.*, 1996). In particular, the complex profiles of dilation and contraction required to warp the atlas onto the new subject's brain provide an index of the anatomical shape differences between that subject's brain and the atlas (Davatzikos *et al.*, 1996). Differences in regional shape can therefore be assessed by the local displacement required to deform one brain volume into another. As a result, deformable atlases not only account for the anatomic variations and idiosyncrasies of each individual subject, they also offer a powerful strategy for exploring and classifying age-related, developmental or pathologic variations in anatomy.

1.1.2. Probabilistic atlases

On the other hand, probabilistic atlasing (Evans *et al.*, 1994; Mazziotta *et al.*, 1995; Thompson *et al.*, 1996a) is a research strategy the goal of which is to generate anatomical templates and expert diagnostic systems which retain quantitative information on inter-subject variations in brain architecture. The recent interest in comprehensive brain mapping also stresses that comparisons between subjects, both within and across homogeneous populations, are required to understand normal variability and genuine structural and functional differences. Initial attempts to derive average representations of neuroanatomy have underscored the validity and power of this approach in both clinical and research settings (Andreasen *et al.*, 1994; Evans *et al.*, 1994). In one such approach, 305 MRI volumes (2 mm thick slices) were mapped by linear transformation into stereotaxic space, intensity normalized and averaged on a voxel-by-voxel basis (Evans *et al.*, 1992). The effect of anatomical variability in different brain areas is illustrated qualitatively by this average-intensity MRI dataset. Nevertheless, the resulting average brain has regions where individual structures are blurred out due to spatial variability in the population (Evans *et al.*, 1992, 1994).

In a recent approach for constructing a probabilistic surface atlas of the brain (Thompson *et al.*, 1996a), a statistical analysis was performed to assess the three-dimensional spatial variation of deep surface structures in the brain (in a reference database of normal scans). Based on this analysis, distributed patterns of abnormality in the same system of anatomic surfaces were quantified and mapped in new subjects. Specifically, connected systems of parametric meshes were used to model several deep internal fissures, or sulci, the trajectories of which represent critical functional and lobar boundaries. Many sulci are comparatively stable in their incidence and connectivity in different individuals. They are also sufficiently extended inside the brain to reflect distributed three-dimensional variations in anatomy between subjects. The parametric form of the system of connected surface elements allowed us to represent the relation between any pair of anatomies as a family of high-resolution displacement maps carrying the surface system of one individual on to another in stereotaxic space. An additional surface analysis algorithm constructed a probability space of random transformations (based on the theory of 3-D Gaussian random fields) reflecting the variability in stereotaxic space of the connected system of anatomic surfaces. Automatic parameterization of the surface anatomy of new subjects enabled the detection and mapping of shape and volume abnormalities in the brains of patients with metastatic tumors. These shape changes were visualized in the form of probability maps on a graphical surface model of the subject's anatomy.

1.2. A hybrid atlasing strategy

1.2.1. A 3-D deformable probabilistic atlas
This paper describes the development of a more comprehensive probabilistic atlas (Figure 1). The technique used in Thompson *et al*. (1996a) quantified anatomic abnormalities in new subjects only on a connected system of surfaces inside their brains. In contrast, we have now devised a strategy for quantifying, mapping and visualizing the anatomic deviations of any given subject not only on an internal surface system, but throughout the entire volume architecture of their brain. To do so, the strategy invokes:

(i) a spatially accurate, anatomically constrained warping algorithm (Thompson and Toga, 1996a), which computes high-dimensional volume deformations, elastically transforming 3-D anatomic images from different subjects and/or modalities into structural correspondence and

(ii) a 3-D probability mapping theory, which generates a visualizable probability measure throughout the 3-D volume of the brain. These probability values quantify the severity of structural abnormalities at a very local level.

A family of high-dimensional volumetric warps relating the new scan to each normal scan in a brain image database is calculated and then used to quantify local structural variations. These warps encode the distribution in a stereotaxic space of anatomic points which correspond across a normal population and their dispersion is used to determine the likelihood of local regions of the new subject's anatomy being in their actual configuration. Any discrepancies can therefore be mapped in three-dimensional space, quantified and evaluated. In deriving the parameters of anatomic variation, the algorithm accounts for the fact that the magnitude of normal anatomic variability, as well as its local directional biases, may differ significantly at every anatomic point in the brain represented in the 3-D image lattice of the new subject's scan. Preliminary results are shown, in which 3-D MRI and high-resolution cryosection volumes were analyzed, from subjects with metastatic tumors and Alzheimer's disease. Gradual variations in the underlying anatomy were also simulated and their dynamic regional effects on the associated probability maps were visualized in the form of graphical animations (see the accompanying video).

Computerized strategies for detecting abnormal structural features in the brain have been very elusive, due to the extraordinary complexity of neuroanatomy and due to the lack of a precise mathematical framework for encoding and retaining information about local variability of structure across homogeneous populations (Grenander and Miller, 1994). Nevertheless, accurate and reproducible detection and classification of anatomic differences remains a topic of much interest in the computer vision and image analysis community. These difficulties have prompted us to explore hybrid approaches in which standard computer vision algorithms and statistical pattern recognition measures are integrated with anatomically driven elastic transformations which encode complex shape differences between systems of anatomic surfaces. Accurate quantitative measurements may then be used to obtain objective criteria for conditions such as global or regional cerebral atrophy and for the assessment of gyral or sulcal anomalies which may be specific to certain disease states (Cook *et al*., 1994; Kikinis *et al*., 1994).

2. METHODS

2.1. Anatomic image acquisition

A multi-modality, multi-subject reference archive of 3-D anatomic images was assembled by imaging many normal subjects with consistent acquisition criteria. Three-dimensional ($384^2 \times 256$ resolution) T_1-weighted fast SPGR (spoiled GRASS) MRI volumes were acquired from 10 normal subjects, on a GE Signa 1.5 T clinical scanner with TR/TE 14.3/3.2 ms, flip angle $35°$, FOV 25 cm and contiguous 1 mm thick slices covering the entire brain. These subjects were age-matched with an identically imaged patient with clinically determined Alzheimer's disease, whose anatomy was analyzed in our first experiment (see Section 3). In addition, six ultra high-resolution ($1024^2 \times 1300 \times 24$ bit) full-color digital cryosection volumes were acquired, as described previously (Toga *et al*., 1994). Six cadavers (age range 72–91 years, three males) were obtained, within 5–10 h post-mortem, through the Willed Body Program at the UCLA School of Medicine. Standard exclusion procedures were applied (Thompson *et al*., 1996b). For our second experiment, an additional cryosection volume was identically acquired, from an age-matched subject with two well-defined metastatic tumors (in the high right putamen and left occipital lobe). Three-dimensional image data from the 18 heads were corrected for differences in relative position and size by transformation into standardized Talairach stereotaxic space, using the steps specified in the Talairach atlas (Talairach and Tournoux, 1988). Control points for the stereotaxic transformation were identified manually in both the high-resolution cryosection and MR volumes, using a 3-D navigation interface (developed by David MacDonald, Montreal Neurological Institute). Alternative, more automated approaches are also under investigation [in particular, the algorithm of Collins *et al*. (1994b)] for the transformation of MR image volumes into standardized Talairach space, with the goal of reducing user intervention and accelerating the registration procedure.

2.2. A generic model of brain geometry using parametric surfaces

2.2.1. Cortical surface extraction

The external cortical surface was extracted automatically from each scan in parametric form, using the 3-D active surface algorithm of MacDonald *et al.* (1993, 1994). Because this algorithm deforms a high-resolution spherical surface mesh into the configuration of the cortex, the resulting model is parametric in the sense that a continuous, invertible one-to-one mapping is always available between points on the cortical surface model and their counterparts on the surface of a sphere. This feature will be invoked in a series of algorithms described in subsequent sections. A range of approaches has been proposed for semi-automatic or automatic extraction of cortical surfaces from high-resolution 3-D MR data (Goble *et al.*, 1994; Sandor and Leahy, 1995; Davatzikos and Bryan, 1996). These methods produce high-resolution shape representations of the cortex, for subsequent visualization and analysis. The 3-D active surface extraction algorithm of MacDonald *et al.* (1993, 1994) has been extensively tested and validated in prior studies (MacDonald *et al.*, 1993, 1994; Holmes *et al.*, 1996). Its ability to extract high-fidelity surface representations of the CSF–gray matter and gray–white matter interfaces in high-resolution MR data has been demonstrated previously (Holmes *et al.*, 1996). In the course of the surface extraction, a spherical mesh surface is continuously deformed, i.e. 'shrink-wrapped', to match a target boundary defined by a threshold value in the continuous 3-D MR image intensity field. The concept is similar to that of a regular net being stretched over an object. The algorithm operates in a multi-scale fashion, so that progressively finer surface detail is extracted at finer scale representations of the data. Initially, both the surface mesh and 3-D intensity field are coarsely sampled and the latter heavily blurred. The initial surface, composed of 8192 polygons, is extracted rapidly, but expresses only the gross shape of the cortex. After several finer scale steps, the data are sampled at 1.0 mm intervals resulting in a surface consisting of 100 000–150 000 polygons (see Figure 5a, and d). The spherical parameterization of the deforming surface is maintained under the complex transformation and the resulting model of the cortex consists of a high-resolution mesh of discrete triangular elements that tile the surface.

2.2.2. Deep surface anatomy

Secondly, since so much of the functional territory of the human cortex is buried in the cortical folds or sulci, we applied a series of recently developed parametric strategies for mapping the internal cortex (Thompson and Toga, 1996b; Thompson *et al.*, 1996a, b). The construction of extremely complex surface deformation maps on the internal cortex is made easier by building a generic structure to model

it (Figure 2). This modeling structure is generic in the anatomical sense, incorporating *a priori* topological and shape information about the deep sulcal pattern. It is also generic in the computational sense, in that the underlying data structure consists of a connected system of surface meshes, in which the individual meshes are parametric and have the form of complex 3-D sheets which divide and join at curved junctions to form a network of connected surfaces. Information on the spatial relations of these meshes, including their surface topology (closed or open), anatomical names, mutual connections, directions of parameterization and common 3-D junctions and boundaries is stored in a hierarchical graph structure [for a powerful related approach see Mangin *et al.* (1995)]. This information is required to ensure the continuity of displacement vector fields and other measures subsequently defined at mesh junctions.

Connected systems of parametric meshes were used to model major lobar, ventricular and cytoarchitectural boundaries in three dimensions. These included complex internal trajectories of the parieto-occipital sulcus, the anterior and posterior calcarine sulcus, the Sylvian fissure and the cingulate, marginal and supracallosal sulci in both hemispheres. The ventricular system was partitioned into a closed system of 14 connected surface elements, the junctions of which reflect cytoarchitectonic boundaries of the adjacent tissue.

2.2.3. Parametric mesh construction

After digital transformation of the 3-D image data into Talairach stereotaxic space, the complex internal paths of the major deep sulcal fissures in each brain were reconstructed using a contour-based system developed in our laboratory (and available at http://www.loni.ucla.edu/loni_code/loni_dist.html), according to the detailed anatomic criteria set out in Steinmetz *et al.* (1989). Additional formal guidelines were devised and applied when identifying the exact course of individual sulci in three dimensions (Thompson *et al.*, 1996b). As in Thompson *et al.* (1996b), the internal trajectory of each sulcus was defined as the medial surface equidistant between the gray–white matter interfaces on either side. Sulcal outlines were digitized as a cursor was moved over a highly magnified image of each slice along the curvilinear path of each sulcus. This resulted in a sampling of ∼15 000 points per structure, capturing the details of each anatomic surface at a very local level. In the future more automated strategies for the extraction and identification of deep cortical folds (Mangin *et al.*, 1995; Le Goualher *et al.*, 1996), sulcal crest lines (Thirion and Gourdon, 1993) and deep sulcal surfaces in parametric form (Vaillant *et al.*, 1996) may facilitate the construction of complex models of deep cortical anatomy.

In the current approach, each surface element, in a connected system of deep cortical folds, was converted into the

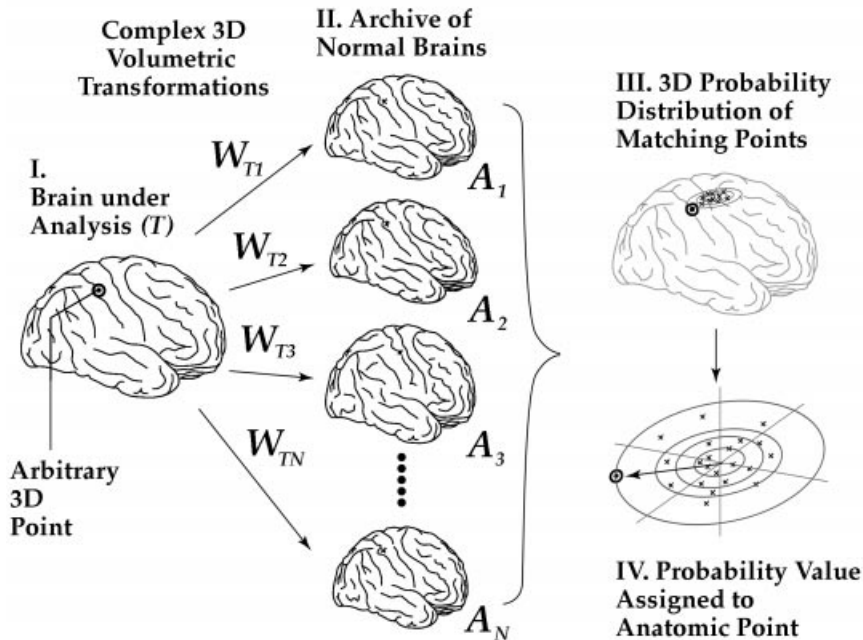## DEFORMABLE PROBABILISTIC ATLAS

Figure 1. Strategy for construction of the brain atlas. A family of high-dimensional volumetric warps relating a new subject's scan to each normal scan in a brain image database is calculated (I, II, above) and then used to quantify local structural variations. Differences in cortical, ventricular and deep sulcal topography are recorded in the form of vector field transformations in 3-D stereotaxic space which drive both subcortical anatomy and the gyral–sulcal patterns of different subjects into register. The resulting family of warps encodes the distribution in stereotaxic space of anatomic points which correspond across a normal population (III) and their dispersion is used to determine the likelihood (IV) of local regions of the new subject's anatomy being in their actual configuration. Easily interpretable, color-coded topographic maps are generated to highlight regional patterns of deformity in the anatomy of the new subject. This approach enables abnormal structural patterns to be quantified locally and mapped in three dimensions.

form of a parametric mesh as previously described (Thompson *et al.*, 1996a, b). Briefly, parameterization of these deep surfaces involves the molding of a linearly elastic lattice-like mesh onto the geometric profile of each surface (Figure 3). The concept is similar to that of a regular net being stretched over an object. Interactive outlining of each sulcal surface S produces an ordered set of cross-sectional contours $C_0, C_1, C_2, \ldots, C_K$ of S, where each contour is itself an ordered set of 3-D digitized points $C_k = \{P_i(x_i^k, y_i^k, z_i^k) | 0 \leq i \leq N_k\}$ in Talairach stereotaxic space. The number of points, N_k, varies for each member, C_k, of the overall stack of contours. Let $\|x - y\|$ denote the distance between 3-D points x and y. To create a mesh of size $I \times J$, we first define, for each C_k, a cumulative arc length $l(p_i^k) = \sum_{j=1 \text{ to } i} \|p_j^k - p_{j-1}^k\|$ to point $p_i^k = P_i(x_i^k, y_i^k, z_i^k)$. For each integer $u = 0$ to I, we also let $i(u) = \min\{i | l(p_i^k) > ul(p_{Nk}^k)/I\}$. A family of K parametric curves is then given by

$$q_u^k = p_{i(u)-1}^k + \lambda(p_{i(u)}^k - p_{i(u)-1}^k),$$

where

$$\lambda = \{(ul(p_{Nk}^k)/I) - l(p_{i(u)-1}^k)\}/\{l(p_{i(u)}^k) - l(p_{i(u)-1}^k)\}.$$

We then let $l_u(q_u^k)$ be the cumulative arc length

$$\sum_{i=1 \text{ to } k} \|q_u^i - q_u^{i-1}\|.$$

For each integer $v = 0$ to J, we let

$$i(v) = \min\{i | l_u(q_u^i) > vl_u(q_K^i)/J\}$$

and

$$\mu = \{(vl_u(q_K^i)/J) - l_u(q_u^{i(v)-1})\}/\{l_u(q_u^{i(v)}) - l_u(q_u^{i(v)-1})\}.$$

Then the 3-D lattice of points

$$r(u, v) = q_u^{i(v)-1} + \mu(q_u^{i(v)} - q_u^{i(v)-1}),$$
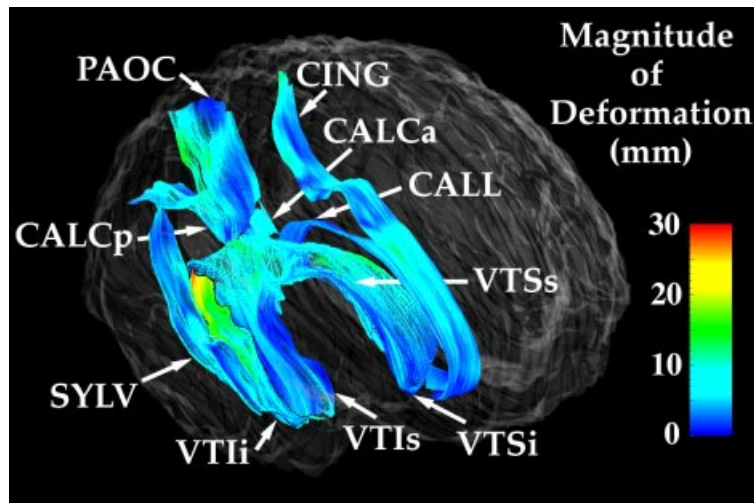$$0 \leq u \leq I, \quad 0 \leq v \leq J,$$

Figure 2. Connected surface systems used to drive the 3-D warp. The complex internal trajectory of the deep structures controlling the deformation field is illustrated here. Deep sulcal surfaces include: the anterior and posterior calcarine (CALCa/p), cingulate (CING), parieto-occipital (PAOC) and callosal (CALL) sulci and the Sylvian fissure (SYLV). Also shown are the superior and inferior surfaces of the rostral horn (VTSs/i) and inferior horn (VTIs/i) of the right lateral ventricle. Ventricles and deep sulci are represented by connected systems of rectangularly parameterized surface meshes, while the external surface has a spherical parameterization which satisfies the discretized system of Euler–Lagrange equations used to extract it. Connections are introduced between elementary mesh surfaces at known tissue-type and cytoarchitectural field boundaries and at complex anatomical junctions (such as the PAOC–CALCa–CALCp junction shown here). Color-coded profiles show the magnitude of the 3-D deformation maps warping these surface components (in the right hemisphere of a 3-D T_1-weighted SPGR MRI scan of an Alzheimer's patient) onto their counterparts in an identically acquired scan from an age-matched normal subject.
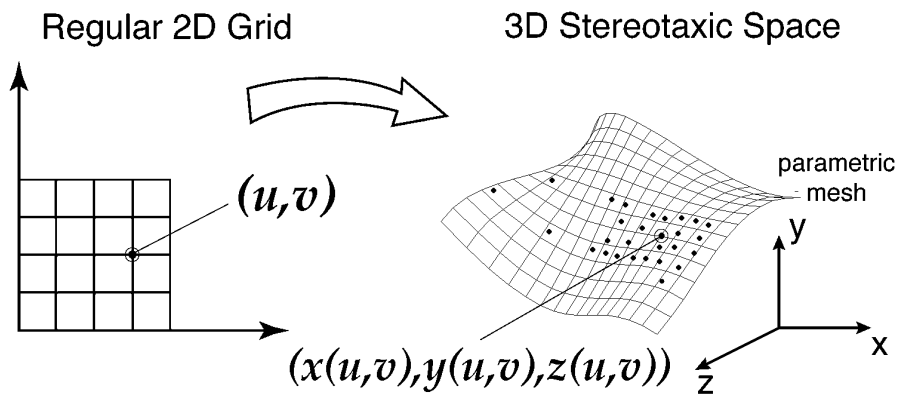

Figure 3. Parametric mesh construction. Comparison and analysis of anatomical models in multiple subjects is facilitated by deriving a standard surface representation of the same type for each corresponding structure. Interactive outlining results in a sampling of $\sim$15 000 points (dots, right-hand panel) located on the boundary of each structure. Although this dense system of points captures the shape details of each anatomic surface at a very local level, their spatial distribution is not quite uniform. To eliminate this dependency, an algorithm (described in the main text) generates a parametric grid of 100×150 uniformly spaced points that act as nodes in a regular rectangular mesh stretched over the surface (right). This scheme provides a means for converting dense systems of points, sampled during outlining, into fully parametric surfaces that can be analyzed, visualized and compared geometrically and statistically.
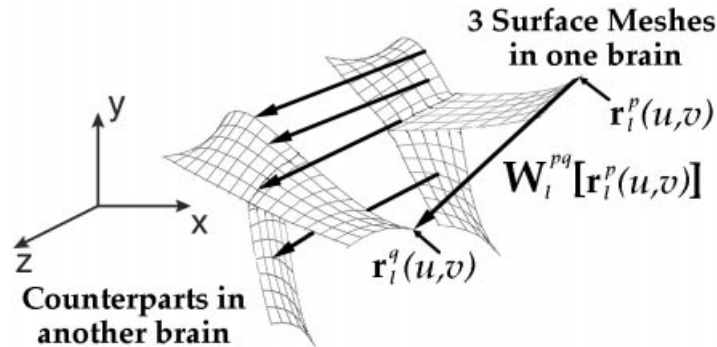
Figure 4. Scheme for matching connected systems of anatomic surfaces. Accurate detection and encoding of anatomic differences between subjects requires transformation tools that deform connected systems of mesh-based surface models (right) representing structures in one subject's anatomy into correspondence with their counterparts (left) in the anatomy of another subject. The computation of this mapping is conceptualized mathematically as a surface-based displacement map, which deforms one system of surfaces into the shape of another. Maintenance of information on surface connectivity guarantees accurate mapping of curved junctions among surfaces, under both the surface-based and subsequent volumetric transformations. Note that matching of surfaces with a spherical parameterization requires the design of separate methods, which deal with the matching of curved internal landmarks. These are detailed in Subsection 2.3.3.

designates the grid points of a regular parametric mesh of size $I \times J$ spanning the sulcal surface S.

Each resultant surface mesh is analogous in form to a uniform rectangular grid, drawn on a rubber sheet, which is subsequently stretched to match all data points. Association of points on each surface with the same mesh coordinate produces a dense correspondence vector field between surface points in different subjects. This procedure is carried out under very stringent conditions (see Subsection 2.2.4), in order to guarantee that the modeling approach has biological as well as computational validity. Constraints on surface parameterizations are designed to ensure that all available anatomical information is incorporated into the model and exploited in driving and constraining the correspondence maps which associate anatomic points in different subjects.

Imposition of an identical regular structure on anatomic surfaces from different subjects (Figure 4) is also required for surface statistics to be derived (Figure 9a). The explicit geometry provided by a parametric mesh-based approach has also proved advantageous for the rapid generation of morphometric statistics from anatomic models derived from normal and diseased populations, as well as quantitative indices of surface curvature, extent, area, fractal dimension and structural complexity (Thompson and Toga, 1996b; Thompson *et al.*, 1996b).

2.2.4. Definition of point correspondences on different surfaces

Much research has been devoted to developing robust methods for defining homology between mesh points, when mesh-based surface models are made to represent anatomical surfaces in different subjects. Parametric mesh approaches, which define a mapping of a 2-D regular grid onto a 3-D surface (Bookstein *et al.*, 1985; Pedersen, 1994) permit cross-subject comparisons to be made by association of different kinds of points (landmark and non-landmark) among geometric forms (Bookstein *et al.*, 1985; see Figure 4). For the comparisons to be valid, several criteria are enforced. First, landmark curves and points known to the anatomist must appear in corresponding locations in each parametric grid. For this reason, the calcarine sulcus (see Figures 2 and 9) was not modeled as a single mesh, but was partitioned into two meshes (CALCa and CALCp); the complex 3-D curve forming their junction with the parieto-occipital sulcus was therefore accurately mapped under both the surface displacement and 3-D volumetric maps, reconfiguring one anatomy into the shape of another. Figure 4 illustrates this procedure in a case where three surface meshes in one brain are matched with their counterparts in a target brain. Exact matching is guaranteed at a three-dimensional junction between the surfaces. This type of method for constraining surface parameterizations, using 3-D free-form landmark curves as constraints, supports both (i) partitioning of parametric elements along landmark curves known to the anatomist and (ii) matching of systems of curves lying within a surface with their counterparts in a target brain. The latter strategy is adopted in Section 3 for bringing gyral regions of the cortex into better alignment. In addition, when mapping a parametric grid from one sulcal surface $r^{(1)}(u, v)$ to its counterpart in another brain $r^{(2)}(u, v)$, a second criterion is enforced. This criterion ensures that the amount of local stretching or contraction of the grid which
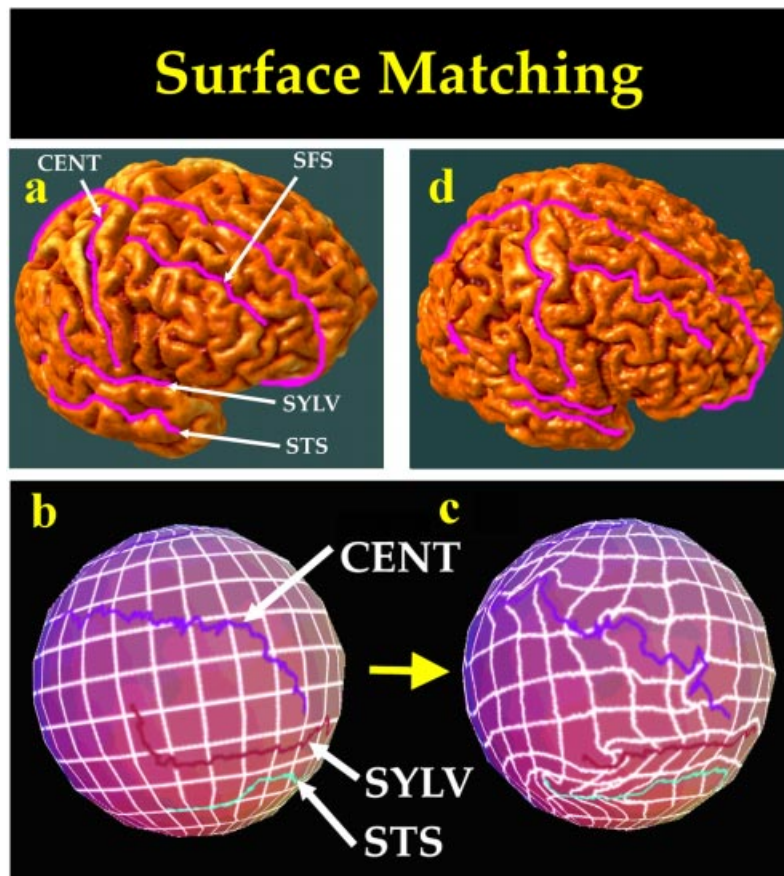
Figure 5. Scheme for matching cortical regions with high-dimensional transformations and color-coded spherical maps. High-resolution surface models of the cerebral cortex were extracted in parametric form, using the active surface algorithm of MacDonald *et al.* (1993, 1994). This means that a continuous, invertible one-to-one mapping is always available between points on the cortical surface (**a**) and their counterparts on the surface of a sphere. No three-dimensional information is lost in this data representation scheme, as each point in the spherical map (**b**) is color-coded with a color value which accurately and uniquely represents the location of its counterpart on the convoluted surface model (a) in 3-D stereotaxic space. (To preserve accuracy, floating point triplets, representing cortical surface point locations in stereotaxic space, are color-coded at 16 bits per channel to form an image of the parameter space in RGB color image format.) To find good matches between cortical regions in different subjects (a and d), we first derive a colorized spherical map for each respective surface model (b and c) and perform the matching process in the angular parametric space. When spherical maps are made from two different cortical surfaces, the respective sulci will be in different positions in each spherical map (b and c), reflecting their different locations on the folded brain surface [shown here in pink, (a and d); curved lines are thickened for visualization purposes only]. Using a complex vector-valued flow field defined on the sphere (**c**), the system of sulcal curves in one spherical map can be driven into exact correspondence with their counterparts in the target spherical map, guiding the transformation of the adjacent regions. A spatially accurate, anatomically driven warping algorithm is used (Thompson and Toga, 1996a), which calculates the high-dimensional deformation field (typically with $65\,536 \times 3 \approx 200\,000$ degrees of freedom) which reconfigures the starting spherical map, and the networks of curves embedded within it, into the shape of their counterparts in the target spherical map. The effect of the transformation is illustrated in (c) by its effect on a uniform grid, ruled over the starting spherical map and passively carried along in the resultant deformation. Notice the complex reconfiguration of sulcal landmarks, and how they drive the deformation of the surrounding cortex, allowing for complex profiles of dilation and contraction of the surface into the shape of the target surface. Complex non-linear flow is observed in superior temporal regions, as the superior temporal sulcus (STS) extends further posteriorly in the target brain and the posterior upswing of the Sylvian fissure (SYLV) is more pronounced in the reference brain (a) than in the target (**d**). Outlines are also shown for the superior frontal sulcus (SFS) and for the central sulcus (CENT) which is far less convoluted in the reference brain than in the target. Because the color-coded spherical maps index cortical surface locations in 3-D, the transformation of one spherical map to another can be recovered in 3-D stereotaxic space as a displacement of points in one subject's cortex onto their counterparts in the cortex of another subject. Matching can therefore be driven by a network of anatomically significant surface features. High spatial accuracy of the match is guaranteed in regions of particular functional significance or structural complexity, such as sulcal curves, lobar and cytoarchitectural boundaries and critical functional landmarks.

results, represented by the scalar field

$$\theta(u, v) = [\|\partial r^{(2)}(u, v)/\partial u\| \cdot \|\partial r^{(2)}(u, v)/\partial v\|]$$
$$\times [\|\partial r^{(1)}(u, v)/\partial u\| \cdot \|\partial r^{(1)}(u, v)/\partial v\|]^{-1},$$

is uniform across the whole surface. The resulting correspondence field $r^{(1)}(u, v) \rightarrow r^{(2)}(u, v)$ between surfaces is unaffected by, and entirely independent of, any global translational or rotational shifts of one surface relative to the other (Thompson *et al.*, 1996a). Experiments conducted and discussed by Thompson *et al.* (1996b) indicate that this surface correspondence algorithm results in an accurate, reproducible, invertible and rotation-invariant method for determining surface correspondence fields. It is by no means the only approach and other powerful techniques have been proposed for matching arbitrary 3-D surfaces based on differential invariants, such as mean and Gaussian curvatures (Feldmar and Ayache, 1994) and crest lines (Monga and Benayoun, 1995). Curvature-based approaches have many advantages in matching curved cortical, ventricular and callosal features (Declerck *et al.*, 1995; Davatzikos, 1996; Davatzikos *et al.*, 1996). The suitability of these differential invariants, across subjects, for matching of deep sulcal surfaces is also under active investigation by ourselves and several other research groups (Joshi *et al.*, 1995a, b; Vaillant *et al.*, 1996). Consistency, across subjects, in sulcal curvature patterns, would be necessary for the success of curvature-based sulcal matching. Variable incidence and numbers of secondary convolutions (Ono *et al.*, 1990) and the lack of a consistent one-to-one map between these features across subjects (e.g. note the morphology of the cingulate sulcus in Figure 8a and b), led us to not adopt curvature-based constraints, in this study, for cross-subject matching of deep sulcal surfaces. Instead, we were encouraged to adopt the uniform surface-dilation approach described above. The correspondence vector field which this defines also sets up a transitive, invertible, equivalence relation on surface points in different subjects. Invertibility properties are advantageous for sulcal matching (Luo and Evans, 1995), because they guarantee that the same pairs of surface points will be matched up by the algorithm in different subjects, regardless of the order in which one scan is warped onto another (Figure 4). Transitivity is also an advantageous property for algorithms which perform surface matching across many subjects. Transitivity guarantees that the same surface points in different scans in the database will be associated, irrespective of which scan is mapped onto the remaining scans in the database to define these correspondences. As well as meeting the additional anatomical criteria described above, this surface matching approach has also been explored, tested and validated statistically in previous studies (Thompson and Toga, 1996a, b; Thompson *et al.*, 1996a, b, c).

2.3. High-dimensional elastic warping driven by parametric surface systems

2.3.1. Overview of the 3-D warping algorithm

Once the surface parameterization and transformation algorithms had been tested and validated on a range of multi-modal image volumes (Thompson *et al.*, 1996a, b), the mathematical theory for a surface-based 3-D warping algorithm was devised (Thompson and Toga, 1996a). This algorithm calculates the high-dimensional deformation field (typically with $384^2 \times 256 \times 3 \approx 10^8$ degrees of freedom) relating the brain anatomies of an arbitrary pair of subjects. Using complex 3-D deformation maps, the connected surface elements in one scan are driven into exact correspondence with their counterparts in a target scan, guiding the transformation of the adjacent brain volume. High spatial acuity of the warp is guaranteed at the surface interfaces used to constrain it and these include many critical functional interfaces such as the ventricles and cortex, as well as numerous cytoarchitectonic and lobar boundaries in three dimensions. The spatial accuracy of the approach was demonstrated on multi-modality real and simulated data in Thompson and Toga (1996a), where full details of the algorithm are presented. Briefly, the algorithm calculates the deformation field required to elastically transform the elements of the surface system in one 3-D image to their counterparts in the target scan. Weighted linear combinations of radial functions, describing the influence of deforming surfaces on points in their vicinity, are then used to extend this surface-based deformation to the whole brain volume.

2.3.2. Matching of deep connected systems of internal surfaces

Let Λ be the image lattice $\{(i, j, k) | 0 \leq i \leq I, 0 \leq j \leq J, 0 \leq k \leq K; I, J, K, i, j, k \in \mathbb{N}\}$ and let $\Omega = \{(u, v) | 0 \leq u \leq U, 0 \leq v \leq V; U, V, u, v \in \mathbb{N}\}$ be the lattice of integer-valued grid points in a rectangular domain of $\mathbb{R}^2$, of fixed size $U \times V$ (for any positive integers U and V). As in Thompson and Toga (1996a), let the lth parametric surface in the nth brain be denoted by the mesh

$$M_l^n = \{r_l^n(u, v) | 0 \leq u \leq U, 0 \leq v \leq V\}.$$

For each of the L different types of anatomic surface, let $\mathcal{F}_l = \{M_l^n, \Omega, N\}$ be the family of N parametric meshes $M_l^n : \Omega \subset \mathbb{R}^2 \rightarrow \mathbb{R}^3$ representing that structure in the N scans $\{A_1, \ldots, A_N\}$ comprising the reference database. For each pair of scans A_p and A_q in the reference database, the goal is to define a 3-D displacement field $W_{pq}(x)$, carrying each surface point $x \in A_p$ into structural correspondence with its anatomic counterpart in A_q, as follows. Firstly, for each surface mesh M_l^p in A_p we define corresponding displacement

maps (Figure 4) on the surfaces, i.e.

$$W_l^{pq}\big[r_l^p(u, v)\big] = r_l^q(u, v) - r_l^p(u, v)$$

(see Subsection 2.2.4).

As illustrated in Figure 4, here $W_l^{pq}[r_l^p(u, v)]$ is a 3-D displacement vector, which, when applied to the mesh point $r_l^p(u, v)$, drives it into correspondence with $r_l^q(u, v)$, which is the point in the target mesh parameterized by rectangular coordinates (u, v).

This family of high-resolution transformations, applied to individual meshes in a connected system deep inside the brain, represents a method for transforming and reconfiguring a deep system of anatomic surfaces in one individual onto their counterparts in a target brain.

2.3.3. Cortical surface matching with high-dimensional transformations and color-encoded spherical maps

The full complexity of the correspondence field which matches two cortical surfaces is considerable; even the sulci which match have arbitrary 3-D trajectories and are embedded in highly convoluted surfaces. Special algorithms are therefore required to define a dense correspondence vector field between scans on the external cortex. To find good matches between cortical regions, we perform the matching process in the cortical surface's spherical parametric space (Thompson and Toga, 1996a; see Figure 5). Approaches using sulcal lines to drive a 3-D volumetric warp are under active investigation in macaque (Joshi *et al.*, 1995a) and human MR data (Banerjee *et al.*, 1995; Declerck *et al.*, 1995; Luo and Evans, 1995), and have been combined with regional intensity correlation to assist in calculating the inter-subject transformation field at the cortical surface (Collins *et al.*, 1996). Our method is conceptually more similar to that of Davatzikos (1996) and is summarized as follows. Three-dimensional active surfaces first produce parametric representations of each subject's cortex, on which corresponding networks of anatomical curves are identified. The transformation relating these networks is expressed as a vector flow field in the parameter space of the cortex. This vector flow field in parameter space indirectly specifies a correspondence field in 3-D, which drives one cortical surface into the shape of another, matching up every element of the specified system of landmark curves, with its counterpart in the target brain.

Because the cortical model is arrived at by the deformation of a spherical mesh [MacDonald *et al.* (1993, 1994); cf. Székely *et al.* (1996) for a discussion of this type of modeling approach], any point on the cortical surface must map to exactly one point on the sphere and vice versa. The location on the sphere corresponding to a surface point defines the parameters of the point; curves on the brain surface (Figure 5a), such as sulci, have exact counterparts on the globe coordinate grid.

Colorized RGB maps of the cortical parameter space. Because surface models of the cerebral cortex were extracted in parametric form, by the continuous deformation of a spherical mesh surface, this means that a continuous, invertible one-to-one mapping is always available between points on the cortical surface (Figure 5a) and their counterparts on the surface of a sphere (Figure 5b). Consequently, all of the sulcal curves and landmarks in the folded brain surface can be reidentified in the spherical map (see Figure 5b), because the spherical map is just an alternative way of representing the brain surface. To avoid loss of three-dimensional information in this data representation scheme, each point in the spherical map (Figure 5b) is color-coded with a color value which accurately and uniquely represents the location of its counterpart on the convoluted surface model (a) in 3-D stereotaxic space. To preserve accuracy, floating point triplets, representing cortical surface point locations in stereotaxic space, are color-coded at 16 bits per channel to form an image of the parameter space in RGB color image format. To find good matches between cortical regions in different subjects (Figure 5a and d), we first derive a spherical map for each respective surface model (Figure 5b and c) and perform the matching process in the spherical parametric space.

Cortical maps. For our current goal, color-coded spherical maps are advantageous for matching cortical regions in different subjects, because the relevant geometric and topological information in the sulcal pattern can be stored in a two-dimensional array structure which supports easy localization of salient features, as well as search and comparison strategies. Much research has also been devoted to computational methods for flattening cortical models into a fully 2-D planar representation (Van Essen and Maunsell, 1980; Schwartz and Merker, 1986; Dale and Sereno, 1993; Carman *et al.*, 1995; Drury *et al.*, 1996b). Faithfully implementing the concept of flattening with all its facets has proved difficult, since the exact Euclidean metric has to be retained along with the flat map to avoid loss of relevant 3-D spatial information about the cortex. For our current purpose, the very difficult issue of creating planar 2-D maps which optimally preserve point-to-point distances is avoided, because the 16-bit color encoding of the spherical map enables measures of in-surface distance between points on the cortex to be computed from the 3-D cortical model directly, rather than from a derived or flattened map of the cortical parameter space.

When colorized spherical maps are made from two different cortical surfaces (Figure 5a and d), the respective sulci will be in different positions in each spherical map, reflecting their different locations on the folded brain surface. Using a complex deformation map (Figure 5c), the system of sulcal curves in one spherical map can be driven into exact correspondence with their counterparts in the target spherical map, guiding the transformation of the adjacent regions. To do this, a spatially accurate, anatomically driven warping algorithm is used (Thompson and Toga, 1996a), which calculates the high-dimensional deformation field (typically with $65\,536 \times 3 \approx 200\,000$ degrees of freedom) which reconfigures the starting spherical map into the shape of the target spherical map. This displacement map is a vector field which matches up major external sulci and is driven by a set of uniformly parameterized external curves, $c_k(t)$. These curves mark critical functional landmarks and lobar boundaries at which deep sulcal surface meshes interface with the automatically extracted external cortex.

Identification of sulcal networks. Because several networks of sulcal curves are used to compute the mapping of one surface onto another, these features must first be identified in high-magnification surface renderings of the cortex of each subject. With the aid of an interactive contouring program (developed by David MacDonald, Montreal Neurological Institute), these sulci were outlined directly using a 3-D navigation interface, on a highly magnified surface-rendered image of each cortical surface. Priority was given to biological features the topological consistency of which has been demonstrated across normal populations (Ono *et al.*, 1990). Three-dimensional curves were drawn to represent (i) the posterior–medial limit of the occipital lobe in each hemisphere, between the parieto-occipital and posterior calcarine sulci; (ii) the inferior limit of the lingual gyrus at the medial wall of each brain hemisphere, from the posterior calcarine sulcus to the splenium of the corpus callosum; (iii) the superior–medial boundary of the parietal lobe, from the parieto-occipital to the central sulcus; (iv) the anterior boundary of the frontal lobes, from the superior–medial limit of the central sulcus to the antero-medial tip of the superior rostral sulcus; (v) the inferior boundary of the frontal lobes, from the superior rostral sulcus posteriorly and inferiorly along the rhinal gyri to the rostral tip of the anterior commissure. As major functional interfaces in the brain, these primary sulci and cortical landmarks were selected because they are easily identifiable, mark critical gyral and lobar boundaries and extend sufficiently far across the cerebral hemispheres to introduce a topological decomposition of their external surface. In addition, their trajectories are sufficiently

extended across the exterior surface of the brain to reflect distributed variations in neuroanatomy between individuals.

As seen in Figure 5, the cortical surface warp from A_p to A_q will have the form

$$(r_p^{\mathrm{C}}, \theta, \phi) + W_{pq}^{\mathrm{C}} = (r_q^{\mathrm{C}*}, \theta + [\Delta\theta(\theta, \phi)], \phi + [\Delta\phi(\theta, \phi)]),$$

where $(r_p^{\mathrm{C}}, \theta, \phi)$ is a point on the cortex of scan p, W_{pq}^{C} is a 3-D displacement vector which takes this point onto the cortical point $(r_q^{\mathrm{C}*}, \theta + [\Delta\theta(\theta, \phi)], \phi + [\Delta\phi(\theta, \phi)])$ in scan q. The parameter shift functions, $\Delta\theta(\theta, \phi)$ and $\Delta\phi(\theta, \phi)$, indicate that corresponding points in different cortical surfaces will, in general, be found at different parameter locations on their respective surfaces. Appropriate parameter shifts are given by the solution to a curve-driven warp in the biperiodic parametric space $(\theta, \phi) \in [0, 2\pi) \times [0, \pi) = \Gamma$ of the external cortex (cf. Davatzikos, 1996; Drury, 1996), using a previously published method (Thompson and Toga, 1996a). Briefly, this method calculates the deformation field required to transform elastically the curved sulcal landmarks in one spherical map (e.g. Figure 5b) into the exact configuration of their counterparts in the target spherical map (e.g. Figure 5c). Spherical harmonic functions, which describe the influence of deforming curves on points in their vicinity, are then used to extend this curve-based deformation to the whole surrounding spherical map. The spatial accuracy of this approach was demonstrated previously (Thompson and Toga, 1996a; Mega *et al.*, 1997) where full details of the algorithm are presented.

One aspect of this transformation not covered in prior work is how the deformation field which transforms one spherical map (and its embedded curve networks) into the configuration of their counterparts in another spherical map, indirectly specifies a correspondence field which matches up points and regions on the convoluted cortical surfaces which the spherical maps represent (Figure 5a and d). Because the spherical maps index cortical surface locations in 3-D, the transformation of one spherical map to another can be recovered in 3-D stereotaxic space as a displacement of points in one subject's cortex onto their counterparts in the cortex of another subject.

This is achieved by computing a series of mathematical mappings, the relationships of which are indicated in Figure 6. If we let $\{x_0, x_1, y_0, y_1, z_0, z_1\}$ represent the extreme (lowest and highest) allowable x, y and z coordinate values for points in Talairach stereotaxic space, then the 3-D stereotaxic locations of cortical surface points in the pth brain are color-encoded in the form of a spherical map, using the invertible function

$$I_p : (x_p, y_p, z_p) \rightarrow (\mathrm{R, G, B}),$$

with 16-bit RGB color channel values given by $R = (2^{16} - 1)(x_p - x_0)/(x_1 - x_0)$, $G = (2^{16} - 1)(y_p - y_0)/(y_1 - y_0)$, $B = (2^{16} - 1)(z_p - z_0)/(z_1 - z_0)$. Since the cortical surface
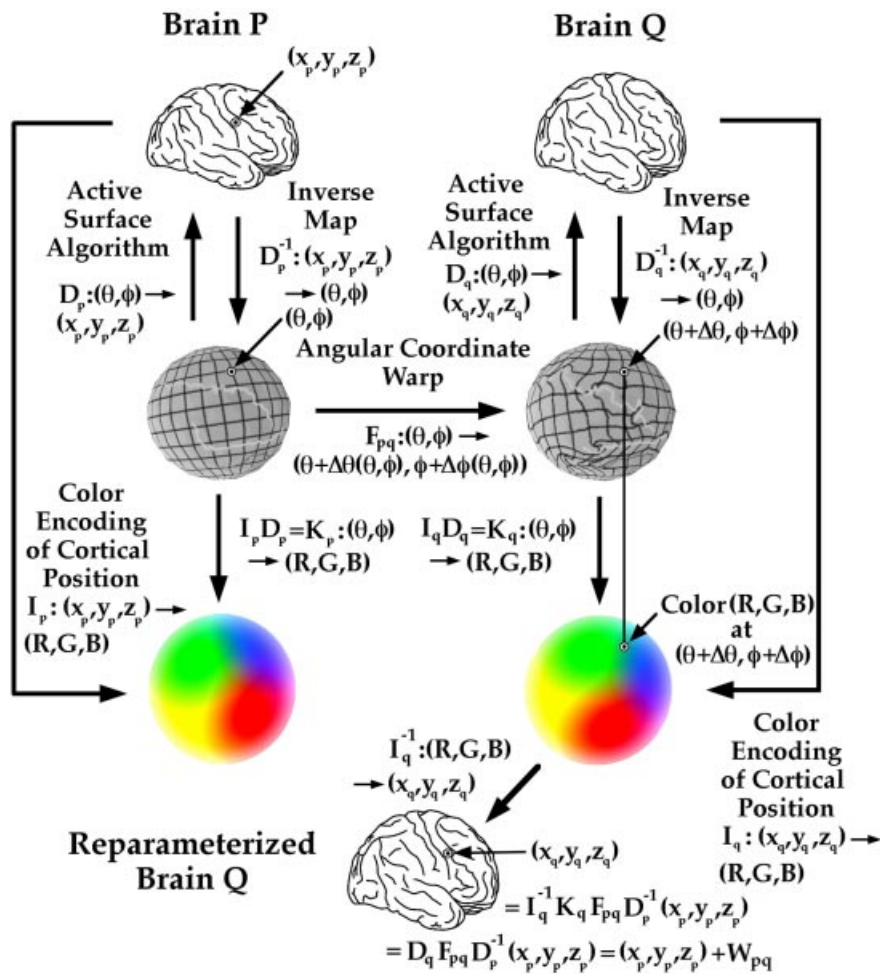
Figure 6. High-dimensional matching of cortical surfaces and sulcal networks. Accurate and comprehensive matching of cortical surfaces requires more than the matching of overall cortical geometry. Connected systems of curved sulcal landmarks, distributed over the cortical surface, must also be driven into correspondence with their counterparts in each target brain. A cascade of mathematical mappings is required to achieve this. Active surface extraction of the cortex provides a continuous inverse mapping from the cortex of each subject to the spherical template used to extract it. Application of these inverse maps (D_p^{-1}, D_q^{-1}) to connected networks of curved sulci in each subject transforms the problem into one of computing an angular flow vector field F_{pq}, in spherical coordinates, which drives the network elements into register on the sphere (Thompson and Toga, 1996a). To greatly accelerate computation of the overall mappings $D_q F_{pq} D_p^{-1}$, the forward mapping D_q, is pre-encoded via the mapping $I_q^{-1} K_q$ as a three-channel floating point array (shown here in color) defined on the co-domain of F_{pq}. The full mapping $D_q F_{pq} D_p^{-1}$ can be expressed as a displacement vector field which drives cortical points and regions in brain P into precise structural registration with their counterparts in brain Q.

extraction algorithm, described earlier, continuously deforms a spherical mesh of points, with initial angular position (θ, ϕ), onto 3-D cortical points with stereotaxic coordinates (x, y, z), we may also represent the extraction of the cortical surface from the pth scan as an invertible mapping $D_p : (\theta, \phi) \rightarrow (x_p, y_p, z_p)$. Then if $K_q : (\theta, \phi) \rightarrow$ (R, G, B) represents the color already assigned by the mapping I_q at angular position

(θ, ϕ) in the spherical map of the qth brain, and if $F_{pq} : (\theta, \phi) \rightarrow (\theta + [\Delta\theta(\theta, \phi)], \phi + [\Delta\phi(\theta, \phi)])$ represents the angular flow field on the sphere calculated for mapping the pth cortical model into the shape of the qth cortical model, then the cortical surface warp W_{pq}^C is given as a displacement map in Cartesian coordinates by the composite mapping

$$(x_p, y_p, z_p) + W_{pq}^C = (x_q, y_q, z_q),$$

where

$$(x_q, y_q, z_q) = I_q^{-1} K_q F_{pq} D_p^{-1}(x_p, y_p, z_p).$$

This sequential procedure is illustrated in Figure 6. Using this method, surface matching can be driven by anatomically significant surface features and the high spatial accuracy of the match is guaranteed in regions of functional significance or structural complexity, such as sulcal curves and cortical landmarks. Consequently, the transformation of one cortical surface model onto another is parameterized by one translation vector for each mesh point in the surface model or $3 \times 65\,536 \approx 0.2 \times 10^6$ parameters. This high-dimensional parameterization of the transformation is required to accommodate the fine anatomical variations (cf. Christensen *et al.*, 1995a).

2.3.4. Systems of surface deformation maps drive the full 3-D volume transformation of one brain onto another

The surface maps described so far drive the full 3-D volume transformation as detailed extensively in Thompson and Toga (1996a). Briefly, for a general voxel $\boldsymbol{x}$ in the scan A_p to be transformed, let $\delta_l^p(\boldsymbol{x})$ be the distance from $\boldsymbol{x}$ to its nearest point(s) on each surface mesh $\boldsymbol{M}_l^p$ and let the scalars $\gamma_l^p(\boldsymbol{x}) \in [0, 1]$ denote the weights $\{1/\delta_l^p(\boldsymbol{x})\}/\sum_{l=1\text{ to }L}\{1/\delta_l^p(\boldsymbol{x})\}$. Then $\boldsymbol{W}_{pq}(\boldsymbol{x})$, the displacement vector which takes a general point $\boldsymbol{x}$ in scan p onto its counterpart in scan q, is given by the linear combination of functions:

$$\boldsymbol{W}_{pq}(\boldsymbol{x}) = \sum_{l=1\text{ to }L} \gamma_l^p(\boldsymbol{x}) \cdot \boldsymbol{D}_l^{pq}(np_l^p(\boldsymbol{x})), \qquad \text{for all } \boldsymbol{x} \in A_p.$$

Here $\boldsymbol{D}_l^{pq}$ are distortion functions (Figure 7) due to the deformation of surfaces close to $\boldsymbol{x}$, given by

$$\boldsymbol{D}_l^{pq}(\boldsymbol{x}) = \left\{ \int_{\boldsymbol{r}\in\boldsymbol{B}(\boldsymbol{x};r_c)} w_l^p(\boldsymbol{x}, \delta_l^p(\boldsymbol{r})) \cdot \boldsymbol{W}_l^{pq}[np_l^p(\boldsymbol{r})] \mathrm{d}\boldsymbol{r} \right\}$$
$$\times \left\{ \int_{\boldsymbol{r}\in\boldsymbol{B}(\boldsymbol{x};r_c)} w_l^p(\boldsymbol{x}, \delta_l^p(\boldsymbol{r})) \mathrm{d}\boldsymbol{r} \right\}^{-1}.$$

$\boldsymbol{W}_l^{pq}[np_l^p(\boldsymbol{r})]$ is the (average) displacement vector assigned by the surface displacement maps to the nearest point(s) $np_l^p(\boldsymbol{r})$ to $\boldsymbol{r}$ on $\boldsymbol{M}_l^p$. R_c is a constant and $\boldsymbol{B}(\boldsymbol{x}; r_c)$ is a sphere of radius $r_c = \min\{R_c, \min\{\delta_l^p(\boldsymbol{r})\}\}$. The w_l^p are additional weight functions defined as

$$w_l^p(\boldsymbol{x}, \delta_l^p(\boldsymbol{r})) = \exp(-\{d(np_l^p(\boldsymbol{r}), \boldsymbol{x})/\delta_l^p(\boldsymbol{x})\}^2),$$

where $d(\boldsymbol{a}, \boldsymbol{b})$ represents the 3-D distance between two points $\boldsymbol{a}$ and $\boldsymbol{b}$. The Jacobian of the transformation field at each point $\boldsymbol{x}$ is tracked during the computation, as recommended

by Christensen *et al.* (1995b)[a]. In rare cases where the transformation is locally singular, the vector field computation is discretized in time and the deformation field is reparameterized at successive time steps, as suggested in Christensen *et al.* (1996). Intermediate surface blends $(1 - t)r_l^p(u, v) + tr_l^q(u, v)$ $(t \in [0, 1])$, are generated for every surface and these surfaces are uniformly reparameterized at times $0 \leq \ldots t_m \prec t_{m+1} \ldots \leq 1$, as described in Subsection 2.2. The M warps mapping the full surface system and surrounding volume from one time point to the next are then concatenated to produce the final transformation. This incremental evolution of the transformation is visualized in the accompanying video (see Section 3). Computational speed is also critical for the practical utility of this algorithm and this issue is addressed at the end of Section 2.4.

Alternative approaches. Experiments conducted and discussed in Thompson and Toga (1996a) indicate that this method for driving a 3-D deformation field with a connected graph of embedded parametric surfaces results in an accurate, reproducible and rotation-invariant algorithm for computing complex vector fields which handle large-magnitude deformations and reconfigure one anatomy into the shape of another. This is by no means the only approach and other powerful methods have been proposed for calculating high-dimensional transformation fields of brain imagery, driven by anatomic features. Declerck *et al.* (1995) express a volume transformation driven by crest lines as a 3-D tensor product of B-spline basis functions. Similarly, Davatzikos (1996) used closed surface models of the ventricles and cortex as anatomical constraints, in a 3-D elastic registration algorithm. In another model, Joshi *et al.* (1995b) demonstrated that a 3-D warping field driven by embedded points, curves and surfaces may also be viewed as the solution of a generalized Dirichlet problem, the precise mathematical form of which depends on the Green's function of the self-adjoint linear operator describing the mechanics of the deforming system. The method presented here was adopted because of its ability to accurately transform complex systems of connected tissue interfaces into structural correspondence with their counterparts in a target brain, respecting complex differences in gyral, cortical and deep sulcal topography from one individual to another (see Figure 8a–c). This type of registration of critical lobar, sulcal and cytoarchitectural boundaries is only possible with a high-dimensional warping technique.

---

[a]The local Jacobian determinant is a scalar field which provides an index of the topological integrity of the deforming template, with values of zero or below indicating that extension of the deformation field from the computation lattice to the continuous domain would not result in a one-to-one transformation of the deforming scan onto the target.
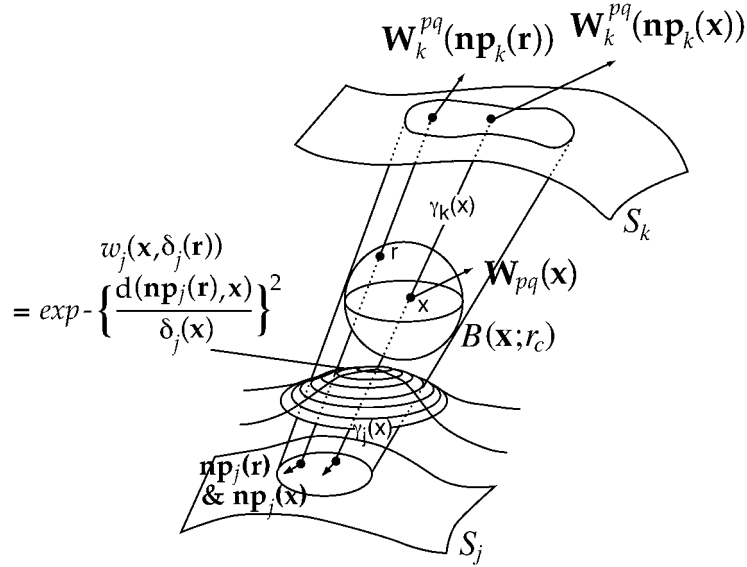
Figure 7. Volume warp calculation. The volumetric transformation $W_{pq}(x)$ of an arbitrary point x in the pth scan to its counterpart in the qth scan is expressed as a weighted linear combination of distortion functions associated with each surface. Within a surface S_i, the relative contribution of each point in the projected patch $\{np_i[B(x; r_c)]\}$ to the elastic transformation at x is given a relative weight w_i. The distortion at x due to surface S_i is given by $D_i^{pq}(x) = \{\int_B w_i W_i^{pq} dr\}/\{\int_B w_i dr\}$, where the W_i^{pq} are the displacement maps defined on each surface (see Subsections 2.3.2 and 2.3.3). The volume warp $W_{pq}(x)$ is a weighted average (over i) of D_i^{pq}, depending on the relative distance $\gamma_i(x)$ of x from its near points on each surface S_i [adapted from Thompson and Toga (1996a)].

2.4. Probability mapping theory

Given a new subject's 3-D brain scan, T, our goal was to assign a probability value $p(x)$ to each anatomic point x in T. This probability value indicates how abnormally situated that point is, given where its counterparts are in the normal scans which make up the database. For increasingly extreme deviations of the anatomic structure at x from its counterparts in the normal scans, the associated probability $p(x)$ of finding the structure there will be correspondingly lower.

Probability values are assigned as the result of a two-stage process, as follows.

(i) For each anatomic point x in the new subject's scan, T, its counterparts are found in the N normal scans (Figure 1, I and II). This is done by calculating the set of warping fields $\{W_{Tn}(x)\}_{n=1 \text{ to } N}$ deforming scan T into structural correspondence with each of the N scans in the database.

(ii) A 3-D probability density function is then recovered from the distribution (in stereotaxic space) of the N points corresponding to x (Figure 1, III). The probability of the anatomic structure at x is then assessed (Figure 1, IV) with reference to the resulting probability distribution.

2.4.1. Three-dimensional spatial variability of anatomy in stereotaxic space

Firstly, let $W_{Tn}(x)$ be the 3-D displacement vector mapping voxel x in the new subject's scan, T, onto its counterpart in the nth brain. Its counterparts in stereotaxic space have a mean position

$$\mu(x) = x + \frac{1}{N} \sum_{n=1 \text{ to } N} W_{Tn}(x),$$

and 3×3 dispersion matrix $\Psi(x)$ whose entries are given by

$$\Psi_{ij}(x) = \left(\frac{1}{N-1}\right) \sum_{n=1 \text{ to } N} |\pi_i W_{n\mu}(x)| \cdot |\pi_j W_{n\mu}(x)|,$$

where $1 \leq i, j \leq 3$ and π_1, π_2, π_3 are orthogonal projections onto each of the three axes of stereotaxic space. Here $W_{n\mu}(x)$ is defined as $\mu(x) - (x + W_{Tn}(x))$ or simply $\mu(x)$ − counterpart$_n(x)$ and can be regarded as the 3-D displacement vector which takes x's counterpart in scan n onto the mean position, or centroid, of x's counterparts in the database. $\Psi(x)$ can be regarded as the covariance matrix of the counterparts of x in the database of normal scans. The diagonal elements $\Psi_{kk} = \sigma_k^2$ are the variances of the x, y and z components of the N volumetric warps $W_{n\mu}(x)$ at x, respectively, and the off-diagonal elements represent the degree of correlation among the components. Then if $W_{n\mu}(x)$ has the multivariate normal
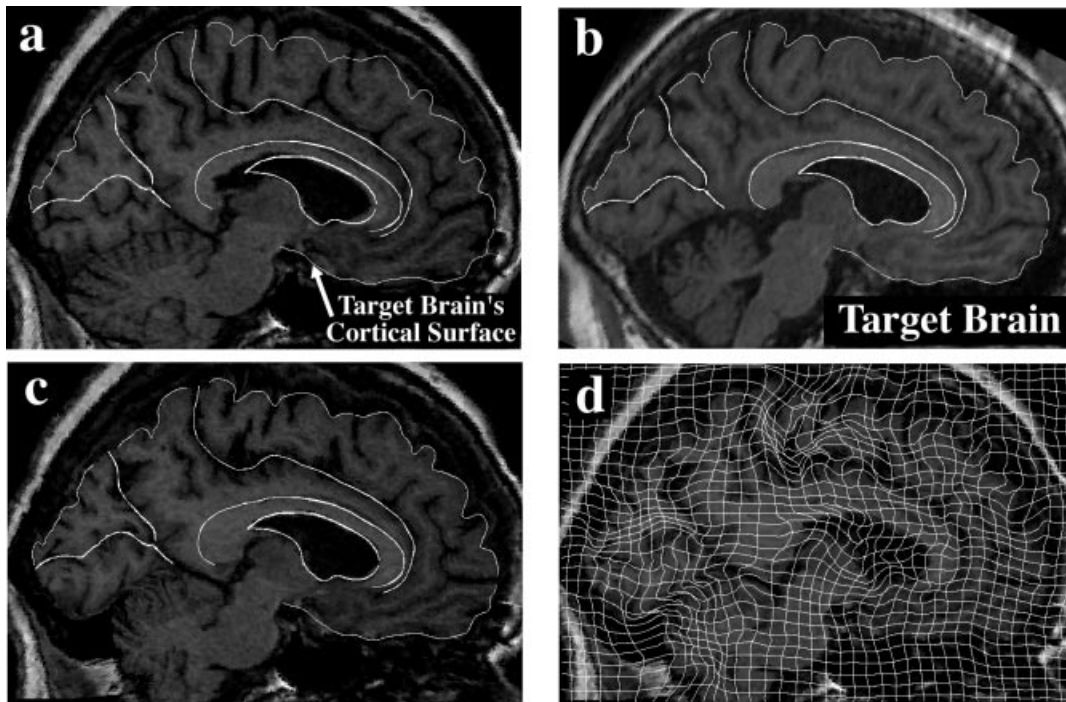
Figure 8. MRI-to-MRI experiment. T_1-weighted MR sagittal brain slice images from (**a**) a randomly selected normal scan from the reference archive; (**b**) the target anatomy, from a patient with clinically determined Alzheimer's disease; (**c**) the result of warping the reference anatomy into structural correspondence with the target. Due to the high degree of cerebellar atrophy, the cerebellar surface was also used to control the deformation in this case. Note the precise non-linear registration of the cortical boundaries, the desired reconfiguration of the major sulci and the contraction of the ventricular space and cerebellum. Both global and local differences in anatomy have been accommodated by the transformation. The complexity of the recovered deformation field is shown by applying the two in-slice components of the 3-D volumetric transformation to a regular grid in the reference coordinate system. This visualization technique (**d**) highlights the especially large contraction in the cerebellar region and the complexity of the warping field in the posterior frontal and cingulate areas, corresponding to subtle local variations in anatomy between the two subjects. To monitor the smooth transition to the surrounding anatomy of the deformation fields initially defined on the surface systems, additional software was developed to visualize the magnitude of the warping field on the surface anatomy of the target brain, as well as on an orthogonal plane slicing through many of these surfaces at the same level as the anatomic sections (**e**). Note the smooth continuation of the warping field from the complex anatomic surfaces into the surrounding brain architecture and the highlighting of the severe deformations in the pre-marginal cortex, ventricular and cerebellar areas. Inter-modality warping: mapping 3-D digital cryosection volumes onto 3-D MRI volumes. The result of warping a randomly selected 3-D cryosectioned image (**f**) into the shape of the target MRI anatomy (b) is shown in (**g**), with cortical and ventricular landmarks of the target anatomy superimposed. Note the degree to which the reference corpus callosum is deformed into the shape of the target corpus callosum. Also, note the reconfiguration (**i**) of the major occipital lobe sulci (**h**) into the shape of the target anatomy. This type of registration of critical lobar, sulcal and cytoarchitectural boundaries would only be possible with a high-dimensional warping technique.

density on $\mathbb{R}^3$ with covariance $\Psi(\boldsymbol{x})$, then even for small N the quantity

$$F(n, \boldsymbol{x}, N) = [N(N-3)/3(N^2-1)]$$
$$\times [\boldsymbol{W}_{n\mu}(\boldsymbol{x})]^{\mathrm{T}} [\Psi(\boldsymbol{x})]^{-1} [\boldsymbol{W}_{n\mu}(\boldsymbol{x})]$$

is an F-distributed variable with 3 and $N-3$ degrees of freedom (Anderson, 1984). Note that this quantity is an F-distributed function which depends not just on the size of the database, N, but also on the number of the scan (n) onto which

the anatomy of the subject under analysis is being warped. It is a measure of how much the point corresponding to $\boldsymbol{x}$ in scan n deviates from the three-dimensional distribution of N points corresponding to $\boldsymbol{x}$ in the entire database.

2.4.2. *Confidence limits for location of neuroanatomic structures in stereotaxic space*

For any desired confidence threshold α, $100(1-\alpha)\%$ confidence regions in stereotaxic space for possible locations of points corresponding to $\boldsymbol{x}$ in $\boldsymbol{T}$ are given by nested ellipsoids
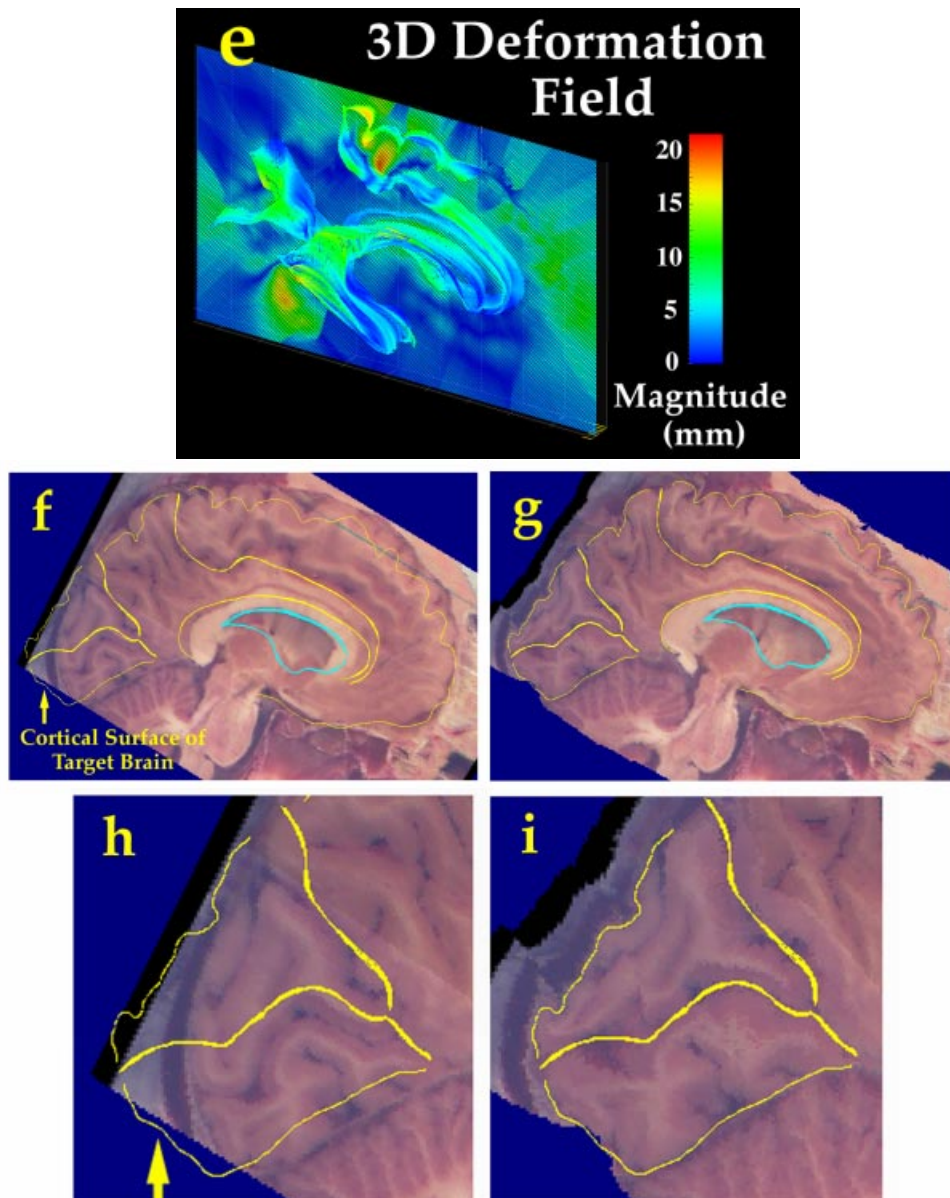
Figure 8. Continued.

$E_{\lambda(\alpha)}(x)$ in displacement space (Thompson *et al.*, 1996a; Figure 1, IV). Here, the ellipsoidal regions, in which a point corresponding to x will occur with probability α in a randomly selected normal subject, have the general form

$$E_{\lambda(\alpha)}(\boldsymbol{x}) = \{\boldsymbol{p} | [\boldsymbol{p} - \mu(\boldsymbol{x})]^{\mathrm{T}} [\Psi(\boldsymbol{x})]^{-1} [\boldsymbol{p} - \mu(\boldsymbol{x})] < \lambda(\alpha)\},$$

where

$$\lambda(\alpha) = [N(N-3)/3(N^2-1)]^{-1} F_{\alpha,3,N-3},$$

and $F_{\alpha,3,N-3}$ is the critical value of the F distribution such that $\Pr\{F_{3,N-3} \geq F_{\alpha,3,N-3}\} = \alpha$. Note that in this expression, while $F_{3,N-3}$ is an F-distributed random variable, the value of $F_{\alpha,3,N-3}$ depends only on α.

2.4.3. *Measuring deviations from normal anatomy*

Finally, we derive a probability measure which expresses how drastically the anatomy found at x in T deviates from its counterparts in the normal scans. If we define $\boldsymbol{W}_{T\mu}(\boldsymbol{x}) = \mu(\boldsymbol{x}) - \boldsymbol{x}$,

the appropriate probability measure, defined throughout the new subject's anatomy, is

$$
\begin{aligned}
p(\boldsymbol{x}) \; = \; & \sup\{\alpha \,|\, F_{\alpha,3,N-3} \geq [N(N-3)/3(N^2-1)] \\
& \times [\boldsymbol{W}_{T\mu}(\boldsymbol{x})]^{\mathrm{T}} [\Psi(\boldsymbol{x})]^{-1} [\boldsymbol{W}_{T\mu}(\boldsymbol{x})]\}, \\
& \forall \boldsymbol{x} \in \boldsymbol{T}.
\end{aligned}
$$

This metric quantifies the severity of local discrepancies $\boldsymbol{W}_{T\mu}(\boldsymbol{x})$ between an anatomic point in a new subject and the 3-D statistical distribution of its counterparts (found by the warping algorithm) in normal anatomic scans which make up the reference database (Figure 1, IV). This closed-form expression, giving the probability measure $p(\boldsymbol{x})$ for each voxel $\boldsymbol{x}$ in the image lattice of the new subject's scan, is evaluated as the limit of an asymptotic series of incomplete gamma functions (Lanczos, 1964), and mapped, via a logarithmic look-up table, on to a standard color range. Probability maps are visualized using Data Explorer 2.1 (IBM Visualization Software). All warping and probability mapping algorithms were written in C and executed on standard 200 MHz DEC Alpha AXP3000 workstations running OSF-1.

2.4.4. Computation speed and efficiency

Accurate quantitative maps, which indicate the severity of deviations from normal anatomy in a convenient graphical form, are easily interpretable and future tests will compare them with more conventional measures of incipient pathology in several clinical scenarios. To be practical, however, these maps must be generated rapidly. This presents a challenge, especially when a family of high-dimensional volumetric maps, taking a subject's image on to each scan in an image database, must be invoked to quantify local variations in brain structure. In practice, the generation of preliminary estimates of transformation fields is accelerated by calculating the deformation fields on a successively refined multi-resolution hierarchy of octree-spline grids (Szeliski and Lavallée, 1993) in the same space as the target image lattice. This hierarchical data structure and multi-resolution strategy permit rapid coarse-to-fine refinement of the deformation field and the generation of intermediate images using 3-D spline interpolation. Within 6–7 min, reasonable estimates of the final deformed images can be generated on demand, for specified slices throughout the warped image volume. As the resolution of the octree-mesh is increased, the algorithm adjusts finer and finer details as subtler differences between the reference and target anatomy are accommodated. A 1152-parameter 3-D spline estimate of the deformation of a single 2-D slice is typically obtained within 240 s on a standard 200 MHz Alpha AXP3000 workstation. 30 min of computation time is required to compute a 6912-parameter estimate of the 3-D deformation field for warping a full volume (calculations being performed on a

regular octree grid of size $16 \times 12 \times 12$). If appropriate hardware is available, several of these computations may be performed simultaneously in parallel. Even on a single processor, though, by restricting the domain on which the computations are defined, probability maps of each anatomical surface in the subject being analyzed can be obtained in considerably less time, typically in 10–12 s per surface mesh or ∼1.5 min for the system of surfaces shown in Figure 9. As the resolution of the computation mesh is successively increased, so is the spatial frequency of the domain on which probability values are defined. Future work will be directed towards the optimization of the component algorithms, with the goal of providing more rapid access to intermediate probability maps which may be updated asymptotically, as the spatial frequency of the underlying computation mesh is successively increased.

3. PRELIMINARY RESULTS

3.1. Visualization of 3-D volumetric transformation fields

A battery of tests was first carried out (Figure 8a–i; Thompson and Toga, 1996b) to evaluate the performance of the warping algorithm on a wide range of real and simulated data. Its capacity to transform images correctly into structural correspondence was investigated by warping different subjects' anatomic images onto each other, both within and across modalities.

Figure 8 shows T_1-weighted MR sagittal brain slice images from (a) a randomly selected normal scan from the reference archive, (b) the target anatomy, from a patient with clinically determined Alzheimer's disease and (c) as a result of warping the reference anatomy into structural correspondence with the target. Parasagittal slices from both 3-D volumes are taken at a level 7.0 mm to the left of the mid-sagittal plane. To emphasize the local differences between the anatomies, several structure boundaries, taken from the same sagittal slice of the target scan, are shown superimposed on the reference scan (a). Major differences are apparent in the extent of the lateral ventricle, as well as differences in cortical boundaries. Note also the smaller cerebellum, less convoluted cingulate sulcus and more ventral position of the posterior calcarine sulcus in the target scan. Figure 8c and d show the result of warping the reference anatomy into the shape of the target. Figure 8d shows the complex effect of the transformation field on a regular grid ruled over the reference anatomy and passively carried along in the resultant deformation. The transformation accommodates both global and local differences in anatomy, ensuring a precise non-linear registration of cortical boundaries, the desired alignment and reconfiguration of major sulci, and the contraction of the ventricular space and the cerebellum. Finally, Figure 8e shows the magnitude of the 3-D deformation
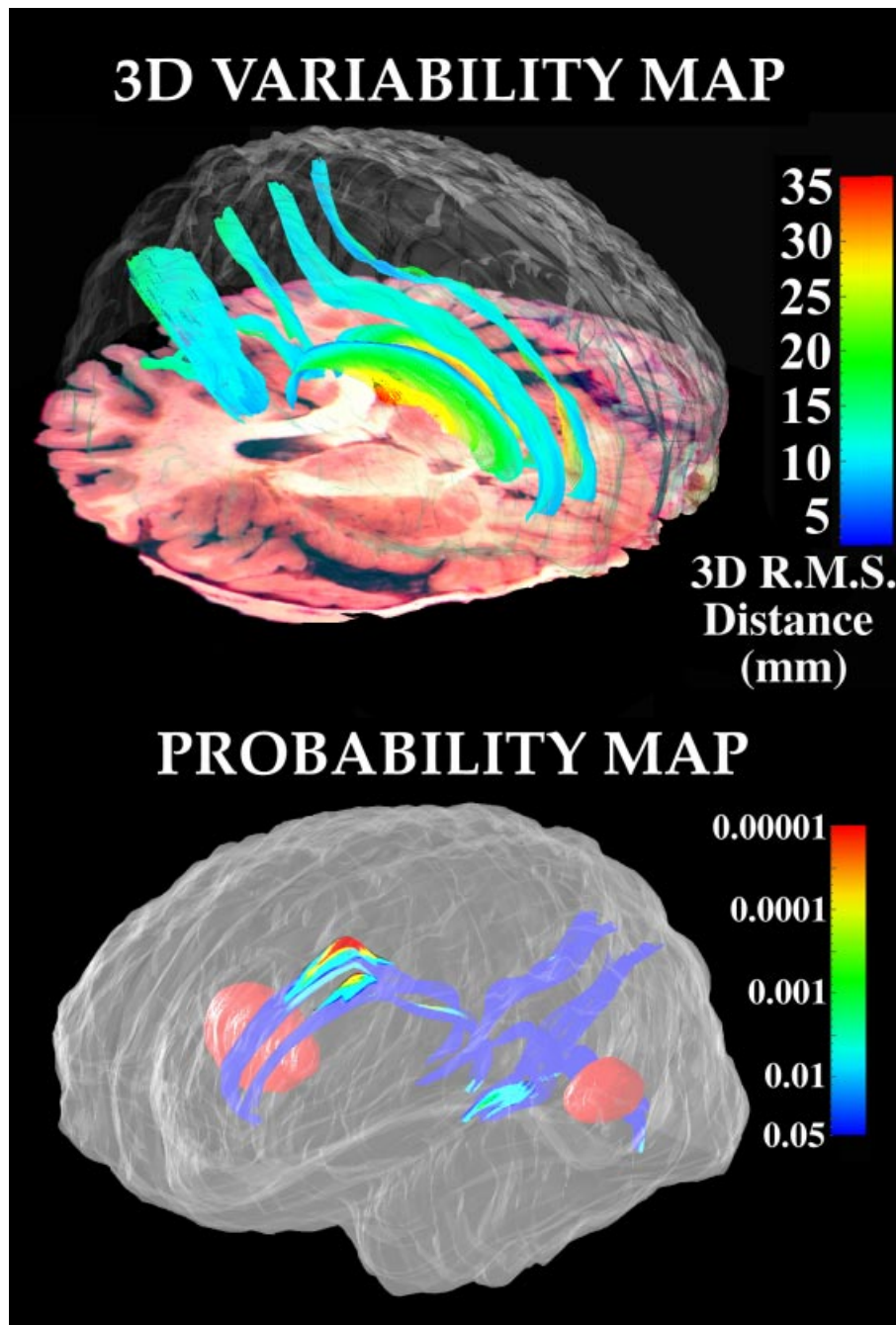
Figure 9. Distortions in brain architecture induced by tumor tissue: probability maps for major sulci in both hemispheres. Top, 3-D RMS variability maps are shown for major occipital and paralimbic sulci; bottom, color-coded probability maps quantify the impact of two focal metastatic tumors (illustrated in red) on the supracallosal, parieto-occipital and anterior and posterior calcarine sulci in both hemispheres.

field in the plane of the anatomic sections, as well as on several elements of the surface system driving the deformation. The warping field exhibits a smooth continuation from the surface systems driving it, into the surrounding architecture of the brain. It also displays considerable complexity in posterior frontal and cingulate areas (see also Figure 8d). Particularly

notable is the pronounced deformation in frontal, ventricular and cerebellar regions, corresponding to local variations in anatomy between the two subjects.

3.2. Inter-modality warping: mapping 3-D digital cryosection volumes onto 3-D MRI volumes

To test the capacity of the algorithm to warp 3-D anatomic imagery acquired in one modality (high-resolution cryosection imaging) onto a target scan from another modality (3-D SPGR MRI), a randomly selected cryosection volume (Figure 8f) was warped into the shape of the target anatomy (Figure 8b) used in the previous experiment. Note, in particular, the degree to which the reference corpus callosum is transformed into the shape of the target callosum. The spatial complexity and continuity properties of this transformation are examined in greater detail on the accompanying video, as described in Subsection 3.4. Complex reconfigurations of cortical regions, such as those observed here most clearly in the occipital lobe (Figure 8h and i), are only possible with high-dimensional warping techniques.

3.3. Probability maps derived from a family of high-dimensional warping fields

As mentioned earlier, the main goal of a deformable probabilistic atlas is to determine whether a subject's anatomy, when compared (by high-dimensional transformation) with matched normal scans in a reference image database, exhibits differences which are statistically unlikely (and hence may constitute a clinical abnormality) or whether they can be explained by normal variations. Random field algorithms are therefore required to understand the full range of normal variability and to help distinguish genuine structural and functional differences. The atlasing strategies developed here incorporate analysis methods which take into account confidence limits on normal variability, as determined from a database of brain images, including non-uniform variability across individual surfaces and volumes in a range of anatomic regions.

As described in Subsection 2.3.2, for each anatomical surface, N different surface meshes have been constructed to represent that surface in N separate individuals, drawn from the image archive. If $r_i(u, v)$ is the 3-D position in stereotaxic space of the point with parametric coordinates (u, v) on the ith person's mesh, then the vector displacement map

$$
\begin{aligned}
d_i(u, v) &= r_i(u, v) - r_\mu(u, v) \\
&= r_i(u, v) - \frac{1}{N} \sum_{j=1 \text{ to } N} r_j(u, v), \\
&\forall (u, v) \in \Omega
\end{aligned}
$$

expresses the ith surface's local deviation from an 'average

mesh', derived from all the subjects in the archive. This map assigns a 3-D displacement vector to each internal surface point. The root mean square magnitude of these displacements, in the N surface maps d_i from individual to average, provides a measure of that surface's variability in stereotaxic space. The values of this function are in millimeters of Talairach space and their range can be linearly mapped via a look-up table onto a color range. Profiles of local variability can therefore be visualized as they vary across each anatomical surface (Figure 9).

Three-dimensional RMS variability maps are shown in Figure 9 for major occipital and paralimbic sulci, as determined from high-resolution image volumes in the cryosection archive. These maps illustrate the ranges of positional variability in stereotaxic space observed for several important functional interfaces in the brain. To illustrate the behavior of the probability mapping algorithms, the brain of a subject with two large, well-defined metastatic tumors, in the high right putamen and left occipital lobe, was cryosectioned and digitally imaged in full color at $1024^2 \times 1300$ pixel resolution and a family of deformation fields was recovered relating their anatomy to that of six identically imaged normal subjects in a reference archive. We emphasize that due to the need for careful age-matching, for this part of the current investigation we focused on a relatively small group of scans from carefully age-matched normal subjects. Accordingly, the statistical framework and probability theory developed here support future expansion of the underlying database and the effects of sample size are taken into account (see Subsections 2.4 and 3.4.3). Future expansion of the reference database will enable us to characterize in detail the effects of different reference populations [such as the group of 10 age-matched subjects with Alzheimer's disease, examined in Thompson *et al.* (1996c)] on measures of regional variability in the brain.

In the anatomy of the cancer patient under analysis, the tumors induced marked distortions in the normal architecture of the brain (Figure 9). Structures in the immediate vicinity of the lesions exhibit probability values three orders of magnitude lower than normal ($p < 0.0001$; red colors), while more distal regions of these structures are normal ($p > 0.05$; deep blue colors). Normal results were obtained for all surfaces ($p > 0.05$; Thompson *et al.*, 1996a), when probability maps were generated for each of the six normal subjects which made up the underlying database. These maps indicate the capacity of the algorithm to appropriately assess structural variants which are within the normal range of variability (Figure 9), without signaling them as regions of potential abnormality. The severity of structural herniation, due to the mechanical effects of a lesion, can also be highlighted and quantified by probability mapping of structures in each hemisphere.

3.4. Video: animation of high-dimensional transformation and probability mapping algorithms used in creating the probabilistic atlas

The accompanying video, which may be found on the CD-ROM included with this journal, illustrates the behavior of some of the warping and probability mapping approaches used in creating the deformable probabilistic atlas.

3.4.1. Animation of high-dimensional image transformations

[0–852 (28 s)[a]]. The kinematics of the continuous elastic deformation of a 3-D cryosectioned brain volume (Figure 9f) into the shape of a target MR volume, shown in Figure 9b, are shown in this animated segment. Notice the complex trajectory of cortical, ventricular and callosal regions as they are elastically reconfigured into the shape of the target anatomy. Recent developments in our laboratory have enabled pre-mortem functional–anatomic scanning and post-mortem cryosection imaging of the same individual (Mega *et al.*, 1997). In these investigations, 3-D warping algorithms, which correct for post-mortem anatomic change, were used to allow direct correlation of 3-D neurochemical and cytoarchitectural maps with 3-D functional (PET) data obtained from the same individual *in vivo*.

3.4.2. Complexity and continuity properties of 3-D deformation fields

[853–1452 (20 s)]. As in Figure 9d, the complexity and continuity of the recovered deformation field in Subsection 3.4.1 are shown by applying the two in-slice components of the 3-D volumetric deformation field to a regular grid in the reference coordinate system. The continuous one-to-one mapping property of the warping transformation keeps all of the structures connected and prevents them from being broken apart. The continuously deforming grid shows dynamically that structures are not broken apart, because the grid lines remain continuous and connected under the evolving transformation.

3.4.3. Dynamic probability mapping: detection and quantification of a series of simulated deformations

[1453–2240 (26 s)]. In this segment, the detection sensitivity of the probability mapping algorithm is investigated by adding deformations of spatially varying magnitude to real anatomical surfaces. In this case, abnormalities are deliberately created and defined mathematically, and the nature and context of the deformations can be varied

[a]The video plays at 30 frames/s; the first set of numbers denote the frame numbers in the video sequence and the number in parentheses denotes the frame playback duration in seconds.

systematically to determine the conditions which affect detection sensitivity.

The anatomy of the subject with two focal metastatic brain tumors (see Subsection 3.3) served as the basis for this experiment. The deformed configuration of their anatomy (Figure 9b) was considered, for simulation purposes, as a severely distorted version of the average representation of anatomy shown in Figure 9a. Linear surface blends were made, for each anatomic surface, and uniformly reparameterized to generate a continuous sequence of intermediate surface models lying between the average anatomy of Figure 9a and the distorted anatomy of Figure 9b. This progressive deformation of the underlying anatomical models was also extrapolated beyond the configuration shown in Figure 9b, to simulate surface deformities which are even more severe than those observed in the anatomy of the tumor patient. Probability maps were then generated for each of the artificially transformed anatomical models. These maps dynamically and continuously reflect the severity of the deformations exhibited by each model, relative to the confidence limits on normal variation determined from the reference image archive.

Probability maps were computed rapidly for the dynamically evolving surface system, using the formula

$$
\begin{aligned}
p_l(u, v, t) = \ & \sup\{\alpha \,|\, F_{\alpha,3,N-3} \ge [N(N-3)/3(N^2-1)] \\
& \times (t^2/f^2)[\boldsymbol{r}_l^*(u, v) - \boldsymbol{r}_{\mu,l}(u, v)]^{\mathrm{T}}[\Psi_l(u, v)]^{-1} \\
& \times [\boldsymbol{r}_l^*(u, v) - \boldsymbol{r}_{\mu,l}(u, v)]\}, \qquad \forall (u, v) \in \Omega.
\end{aligned}
$$

$p_l(u, v, t)$ is the probability value assigned to the lattice point (u, v) in the lth parametric surface mesh at time t. t is the frame number (in this animation) and f is the frame rate, chosen so that $0 \le \ldots t_m/f \prec t_{m+1}/f \ldots \le 2$. $\boldsymbol{r}_{\mu,l}$ and $\boldsymbol{r}_l^*$ denote the lth surface mesh in the average anatomy of Figure 9a and the distorted anatomy of Figure 9b, respectively. $F_{\alpha,3,N-3}$ is the critical value of the F distribution with 3 and $N-3$ degrees of freedom such that $\Pr\{F_{3,N-3} \ge F_{\alpha,3,N-3}\} = \alpha$, N is the size of the reference image archive and $\Psi_l(u, v)$ is the dispersion matrix of the stereotaxic locations of the N surface points at parameter location (u, v) in the lth surface mesh, for each subject in the reference archive. This closed-form expression was evaluated recursively at each mesh point by expansion in terms of incomplete gamma functions, the computation of which was accelerated using asymptotic series representations due to Lanczos (1964).

These data illustrate the graded response of the probability mapping algorithm in assessing deformations of spatially varying magnitude across complex systems of connected anatomic surfaces. They also indicate the capacity of the algorithm to assess appropriately structural variants which are within the normal range of variability (cf. Figure 9a), without

signaling them as regions of potential abnormality. Finally, one very desirable property for characterizing the potential severity of anatomic abnormalities is that the probability measure decreases, in a monotonic way, with the magnitude of structural deformation. This feature is reflected in the sequence of probability maps constructed here.

4. CONCLUSION

The high-dimensional warping and probabilistic mapping approaches developed here provide a framework for visualizing complex structural variations in the anatomy of new subjects. Preliminary data have illustrated the feasibility of creating probability maps on surface systems, which typically consist of critical structural and functional interfaces and boundaries in three dimensions. We have also described a method for calculating probability maps throughout the full volume of a subject's brain to provide a more comprehensive measure of distributed patterns of structural abnormality. The extension of a probability measure from surfaces to volumes requires the development of an additional algorithm, with almost unlimited degrees of freedom, to transform a scan into structural correspondence with each scan in an image archive. The capacity of this algorithm to estimate the locations of classes of points which correspond across a range of image volumes allows us to characterize the statistical dispersion of these points in stereotaxic space. Algorithms defined on the archive of anatomic data can readily use the family of associated warping fields to produce probability distributions and confidence limits for structure identification. Deviations in the anatomy of new subjects can therefore be analyzed and quantified at an extremely local level. Anisotropic random fields, invoked in the generation of probability maps for new subjects, readily encode local biases in the direction of anatomic variability (Figure 9) and hence quantify the severity of anatomic deviations more effectively than simple distance-based descriptors (Figure 8d and e).

In the future, probabilistic atlases of the human brain, which encode information on structural variability, may provide a better understanding of the complex regional changes which occur under a variety of normal and pathological conditions. Accurate quantitative measurements may ultimately be used to obtain objective criteria for conditions such as global or regional cerebral atrophy (Thompson *et al.*, 1997) and for the assessment of gyral or sulcal anomalies which may be specific to certain disease states.

The surface-based modeling, mapping and warping approaches presented in this paper may offer distinct advantages over volume averaging for statistical atlasing applications. Surface representations lend themselves readily to averaging and subsequent statistical characterization. More particularly

though, the averaging procedure itself does not lead to the same type of degradation of structural geometry (and loss of fine anatomic features) as is often apparent when image volumes are directly averaged, without high-dimensional registration.

In addition, the retention of an explicit surface topology after averaging is particularly advantageous for subsequent visualization (Thompson and Toga, 1996a; Thompson *et al.*, 1996a). This feature of both the individual and average representations of brain anatomy enables secondary regional information, including local probability maps, to be overlaid and visualized on the underlying surface models (Sclaroff, 1991). Information about physiology, neurochemistry, and an infinite variety of relevant maps can potentially be layered onto the anatomic atlas and referenced using such a system. In the brain, such surface maps include cytoarchitecture, chemoarchitecture, blood-flow distributions and metabolic rates.

Strictly speaking, some anatomical detail is lost in surface-based methods, since deformable surface models are used for regularization and resampling of anatomical surfaces. Regularization is directly analogous to filtering (Nielsen *et al.*, 1994), a feature which has been used to great effect in a recent fast fluid registration approach (Bro-Nielsen and Gramkow, 1996). However, experiments conducted in Holmes *et al.* (1996) suggest that regularized surface models may reflect the brain's surface topography closely enough to determine maps of cortical thickness; tests conducted by Thompson *et al.* (1996b) also suggest that deep surface meshes, even derived from manually traced contours, can be accurately reproduced in separate trials with a spatial variability 30–80 times smaller than the range of normal inter-subject variability.

In the future, probabilistic mapping is likely to be fundamental to multi-subject atlasing and many other brain mapping projects. Digital probabilistic atlases based on large populations will rectify many current atlasing problems, since they retain quantitative information on the variability inherent in anatomic populations. As the underlying database of subjects increases in size and content, the digital, electronic form of the atlas provides efficiency in statistical and computational comparisons between individuals or groups. The atlas also improves in accuracy over time, achieving better statistics as more information is added to the underlying database. Finally, the source data on which probabilistic atlases are based may be stratified into subpopulations by age, gender, by stage of development (Toga *et al.*, 1996) or to represent different disease types (Thompson *et al.*, 1996c).

The ultimate goal of brain mapping is to provide a framework for integrating functional and anatomical data across many subjects and modalities. This task requires precise quantitative knowledge of the variations in geometry and location of intracerebral structures and critical functional

interfaces. The high-dimensional warping and probabilistic techniques presented here provide a basis for the generation of anatomical templates and expert diagnostic systems which retain and exploit quantitative information on inter-subject variations in brain architecture.

ACKNOWLEDGEMENTS

REFERENCES

Anderson, T. W. (1984) *An Introduction to Multivariate Statistical Analysis*. Wiley, New York.

Andreasen, N. C., Arndt, S., Swayze, V., Cizadlo, T., Flaum, M., O'Leary, D., Ehrhardt, J. C. and Yuh, W. T. C. (1994) Thalamic abnormalities in schizophrenia visualized through magnetic resonance image averaging. *Science*, 266, 294–298.

Banerjee, A., Christensen, G. E., Haller, J. W., Joshi, S. C., Raichle, M. E. and Miller, M. I. (1995) Accommodating anatomical variability in functional imaging via deformable templates. *Proc. 33rd Ann. Allerton Conf. on Communications, Control and Computing*, University of Illinois, Urbana-Champaign, IL, pp. 275–284.

Bookstein, F. L., Chernoff, B., Elder, R., Humphries, J., Smith, G. and Strauss, R. (1985) *Morphometrics in Evolutionary Biology*, Special Publication 15, Academy of Natural Sciences of Philadelphia, Philadelphia, PA.

Bro-Nielsen, M. and Gramkow, C. (1996) Fast fluid registration of medical images. In Höhne, K. H. and Kikinis, R. (eds), *Visualization in Biomedical Computing*, Hamburg, *Lecture Notes in Computer Science*, Vol. 1131, pp. 267–276. Springer-Verlag, Berlin.

Carman, G. J., Drury, H. A. and Van Essen, D. C. (1995) Computational methods for reconstructing and unfolding the cerebral cortex. *Cerebral Cortex*, 5, 506–517.

Christensen, G. E., Rabbitt, R. D. and Miller, M. I. (1993) A deformable neuroanatomy textbook based on viscous fluid mechanics. *27th Ann. Conf. on Information Sciences and Systems*, Johns Hopkins University, Baltimore, MD, March 24–26, pp. 211–216.

Christensen, G. E., Miller, M. I., Marsh, J. L. and Vannier, M. W. (1995a) Automatic analysis of medical images using a deformable textbook. *Proc. Computer Assisted Radiology 1995*, Berlin, Germany, June 21–24, pp. 152–157. Springer-Verlag, Berlin.

Christensen, G. E., Rabbitt, R. D., Miller, M. I., Joshi, S. C., Grenander, U., Coogan, T. A. and Van Essen, D. C. (1995b) Topological properties of smooth anatomic maps. In Bizais, Y., Barillot, C. and Di Paola, R. (eds), *Information Processing in Medical Imaging*, pp. 101–112.

Christensen, G. E., Rabbitt, R. D. and Miller, M. I. (1996) Deformable templates using large deformation kinematics. *IEEE Trans. Image Process.*, 5, 1435–1447.

Collins, D. L., Peters, T. M. and Evans, A. C. (1994a) An automated 3D non-linear image deformation procedure for determination of gross morphometric variability in the human brain. *Proc. Visualization in Biomedical Computing*, SPIE, Vol. 3, pp. 180–190.

Collins, D. L., Neelin, P., Peters, T. M. and Evans, A. C. (1994b) Automatic 3D intersubject registration of MR volumetric data into standardized Talairach space. *J. Comput. Assis. Tomogr.*, 18, 192–205.

Collins, D. L., Le Goualher, G., Venugopal, R., Caramanos, A., Evans, A. C. and Barillot, C. (1996) Cortical constraints for non-linear cortical registration. In Höhne, K. H. and Kikinis, R. (eds), *Visualization in Biomedical Computing*, Hamburg, *Lecture Notes in Computer Science*, Vol. 1131, 307–316. Springer-Verlag, Berlin.

Cook, M. J., Free, S. L., Fish, D. R., Shorvon, S. D., Straughan, K. and Stevens, J. M. (1994) Analysis of cortical patterns. In Shorvon, S. D. (ed.), *Magnetic Resonance Scanning and Epilepsy*, pp. 263–274. Plenum, New York.

Dale, A. M. and Sereno, M. I. (1993) Improving localization of cortical activity by combining EEG and MEG with MRI cortical surface reconstruction: a linear approach. *J. Cogn. Neurosci.*, 5, 162–176.

Davatzikos, C. (1996) Spatial normalization of 3D brain images using deformable models. *J. Comput. Assis. Tomogr.*, 20, 656–665.

Davatzikos, C. and Bryan, R. N. (1996) Using a deformable surface model to obtain a shape representation of the cortex. *IEEE Trans. Med. Imag.*, 15, 785–795.

Davatzikos, C., Vaillant, M., Resnick, S. M., Prince, J. L., Letovsky, S. and Bryan, R. N. (1996) A computerized approach for morphological analysis of the corpus callosum. *J. Comput. Assis. Tomogr.*, 20, 88–97.

Declerck, J., Subsol, G., Thirion, J.-P. and Ayache, N. (1995) Automatic retrieval of anatomical structures in 3D medical images. In Ayache, N. (ed.), *CVRMed'95*, Nice, *Lecture Notes in Computer Science*, Vol. 905, pp 153–162. Springer-Verlag, Berlin.

Drury, H. A. (1996) Analysis and comparison of areal partitioning schemes using two-dimensional fluid deformations. Poster Presentation, *2nd Int. Conf. on Functional Mapping of the Human Brain*, Boston, MA.

Drury, H. A., Van Essen, D. C., Anderson, C. H., Lee, C. W., Coogan, T. A. and Lewis, J. W. (1996) Computerized mappings of the cerebral cortex: a multiresolution flattening method and a surface-based coordinate system. *J. Cogn. Neurosci.*, 8, 1–28.

Evans, A. C., Dai, W., Collins, L., Neelin, P. and Marrett, S. (1991) Warping of a computerized 3D atlas to match brain image volumes for quantitative neuroanatomical and functional analysis. *Proc. Int. Soc. Opt. Eng. (SPIE): Medical Imaging III*, pp. 264–274.

Evans, A. C., Collins, D. L. and Milner, B. (1992) An MRI-based stereotactic brain atlas from 300 young normal subjects. In *Proc. 22nd Symp. Society for Neuroscience*, Anaheim, p. 408.

Evans, A. C., Kamber, M., Collins, D. L. and MacDonald, D. (1994) An MRI-based probabilistic atlas of neuroanatomy. In Shorvon, S. D. *et al.* (eds), *Magnetic Resonance Scanning and Epilepsy*, pp. 263–274. Plenum Press, New York.

Feldmar, J. and Ayache, N. (1994) Rigid, Affine, and locally Affine registration of free-form surfaces, *Technical Report* 2220, INRIA, France.

Gee, J. C., Reivich, M. and Bajcsy, R. (1993) Elastically deforming an atlas to match anatomical brain images. *J. Comput. Assis. Tomogr.*, 17, 225–236.

Goble, J. C., Snell, J. W. and Katz, W. T. (1994) Semi-automatic model-based segmentation of the brain from magnetic resonance images. In *AAAI, Applications of Computer Vision in Medical Image Processing, Spring Symp. Series*, pp. 211–214. Stanford University, Stanford, CA.

Greitz, T., Bohm, C., Holte, S. and Eriksson, L. (1991) A computerized brain atlas: construction, anatomical content, and some applications. *J. Comput. Assis. Tomogr.*, 15, 26–38.

Grenander, U. and Miller, M. I. (1994) Representations of knowledge in complex systems. *J. R. Stat. Soc.* B, 56, 549–603.

Höhne, K.-H., Bomans, M., Riemer, M., Schubert, R., Tiede, U. and Lierse, W. (1992) A 3D anatomical atlas based on a volume model. *IEEE Comp. Graphics Appl.*, 12, 72–78.

Holmes, C. J., MacDonald, D., Sled, J. G., Toga, A. W. and Evans, A. C. (1996) Cortical peeling: CSF/grey/white matter boundaries visualized by nesting isosurfaces. *Proc. Visualization Biomed. Comp.*, 4, 99–104.

Joshi, S. C., Wang, J., Miller, M. I., Van Essen, D. C. and Grenander, U. (1995a) On the differential geometry of the cortical surface. *Vision Geometry IV, Proc. SPIE Conf. on Optical Science, Engineering and Instrumentation*, San Diego, CA, Vol. 2573, pp. 304–311.

Joshi, S. C., Miller, M. I., Christensen, G. E., Banerjee, A., Coogan, T. A. and Grenander, U. (1995b) Hierarchical brain mapping via a generalized Dirichlet solution for mapping brain manifolds. *Vision Geometry IV, Proc. SPIE Conf. on Optical Science, Engineering and Instrumentation*, San Diego, CA, Vol. 2573, pp. 278–289.

Kikinis, R., Shenton, M. E., Gerig, G., Hokama, H., Haimson, J., O'Donnell, B. F., Wible, C. G., McCarley, R. W. and Jolesz, F. A. (1994) Temporal lobe sulco-gyral pattern anomalies in schizophrenia: an *in vivo* MR three-dimensional surface rendering study. *Neurosci. Lett.*, 182, 7–12.

Kikinis, R., Shenton, M. E., Iosifescu, D. V., McCarley, R. W., Saiviroonporn, P., Hokama, H. H., Robatino, A. Metcalf, D., Wible, C. G., Portas, C. M., Donnino, R. and Jolesz, F. (1996) A digital brain atlas for surgical planning, model-driven segmentation, and teaching. *IEEE Trans. Visualization Comp. Graphics*, 2, 232–241.

Lanczos, D. (1964) Numerical analysis. *J. SIAM*, 1, 86.

Le Goualher, G., Barillot, C., Bizais, Y. and Scarabin, J.-M, (1996) 3D segmentation of cortical sulci using active models. *SPIE Med. Imag.*, 2710, 254–263.

Luo, S. and Evans, A. C. (1995) A method to match human sulci in 3D space. *Proc. IEEE 17th Ann. Conf. on Engineering in Medicine and Biology*, Section 2.1.2(14).

MacDonald, D., Avis, D. and Evans, A. C. (1993) Automatic parameterization of human cortical surfaces. *Ann. Symp. Information Processing in Medical Imaging (IPMI)*.

MacDonald, D., Avis, D. and Evans, A. C. (1994) Multiple surface identification and matching in magnetic resonance imaging. *Proc. SPIE*, 2359, 160–169.

Mangin, J.-F., Frouin, V., Bloch, I., Regis, J. and López-Krahe, J. (1995) From 3D magnetic resonance images to structural representations of the cortex topography using topology-preserving deformations. *J. Math. Imag. Vision*, 5, 297–318.

Mazziotta, J. C., Toga, A. W., Evans, A. C., Fox, P. and Lancaster, J. (1995) A probabilistic atlas of the human brain: theory and rationale for its development. *NeuroImage*, 2, 89–101.

Mega, M. S., Chen, S. S., Thompson, P. M., Woods, R. P., Karaca, T. J., Tiwari, A., Vinters, H. and Toga, A. W. (1997) Mapping histology to metabolism: coregistration of stained whole brain sections to premortem PET using 3D cryomacrotome reconstruction as a reference. *NeuroImage*, in press.

Monga, O. and Benayoun, S. (1995) Using partial derivatives of 3D images to extract typical surface features. *Comp. Vision Image Understanding*, 61, 171–189.

Nielsen, M., Florack, F. and Deriche, R. (1994) Regularization and scale space. *INRIA Technical Report*, 2352.

Ono, M., Kubik, S. and Abernathey, C. (1990) *Atlas of the Cerebral Sulci*. Thieme, Stuttgart.

Pedersen, H. K. (1994) Displacement mapping using flow fields. In *Proc. 1994 SIGGRAPH Computer Graphics Conf.*, pp. 279–286.

Rabbitt, R. D., Weiss, J. A., Christensen, G. E. and Miller, M. I. (1995) Mapping of hyperelastic deformable templates using the finite element method. *Proc. SPIE*, 2573, 252–265.

Roland, P. E. and Zilles, K. (1994) Brain atlases—a new research tool. *Trends Neurosci.*, 17, 458–467.

Sandor, S. R. and Leahy, R. M. (1994) Matching deformable atlas models to pre-processed magnetic resonance brain images. *Proc. 3rd IEEE Conf. on Image Processing*, pp. 686–690.

Sandor, S. R. and Leahy, R. M. (1995) Towards automated labeling of the cerebral cortex using a deformable atlas. In Bizais, Y., Barillot, C. and Di Paola, R. (eds), *Info. Proc. in Medical Imaging*, pp. 127–138.

Schwartz, E. L. and Merker, B. (1986) Computer-aided neuroanatomy: differential geometry of cortical surfaces and an optimal flattening algorithm. *IEEE Comp. Graphics Appl.*, 6, 36–44.

Sclaroff, S. (1991) Deformable solids and displacement maps: a multi-scale technique for model recovery and recognition. *Master's Thesis*, MIT Media Laboratory, MA.

Steinmetz, H., Furst, G. and Freund, H.-J. (1989) Cerebral cortical localization: application and validation of the proportional grid system in MR imaging. *J. Comput. Assis. Tomogr.*, 13, 10–19.

Székely, G., Kelemen, A., Brechbühler, C. and Gerig, G. (1996) Segmentation of 2D and 3D objects from MRI volume data using constrained elastic deformations of flexible fourier contour and surface models. *Med. Image Anal.*, 1, 19–34.

Szeliski, R., Lavallée, S. (1993) Matching 3D anatomic surfaces with non-rigid deformations using octree-splines. *Geometric Methods in Computer Vision II*, *SPIE*, Vol. 2031, pp. 306–315.

Talairach, J. and Tournoux, P. (1988) *Co-planar Stereotaxic Atlas of the Human Brain*. Thieme Medical Publishers, New York.

Thirion, J.-P. (1995) Fast non-rigid matching of medical images. *INRIA Internal Report* 2547, Projet Epidaure, INRIA, France.

Thirion, J.-P. and Gourdon, A. (1993) The Marching lines algorithm: new results and proofs. *INRIA Internal Report* 1881, Projet Epidaure, INRIA, France.

Thompson, P. M. and Toga, A. W. (1996a) A surface-based technique for warping 3-dimensional images of the brain. *IEEE Trans. Med. Imag.*, 15, 1–16.

Thompson, P. M. and Toga, A. W. (1996b) Mapping the internal cortex: a probabilistic brain atlas based on random fluid transformations. Poster Presentation, *2nd Int. Conf. on Functional Mapping of the Human Brain*, Boston, MA.

Thompson, P. M., Schwartz, C. and Toga, A. W. (1996a) High-resolution random mesh algorithms for creating a probabilistic 3D surface atlas of the human brain. *NeuroImage*, 3, 19–34.

Thompson, P. M., Schwartz, C., Lin, R. T., Khan, A. A. and Toga, A. W. (1996b) 3D statistical analysis of sulcal variability in the human brain. *J. Neurosci.*, 16, 4261–4274.

Thompson, P. M., Mega, M. S., Moussai, J., Zohoori, S., Xu, L. Q., Goldkorn, A., Khan, A. A., Coryell, J., Small, G., Cummings, J. and Toga, A. W. (1996c) 3D probabilistic atlas and average surface representation of the Alzheimer's brain, with local variability and probability maps of ventricles and deep cortex. In *Proc. 1996 Symp. of the Society for Neuroscience*, Washington, DC, Vol. 26, p. 1105.

Thompson, P. M., MacDonald, D., Mega, M. S., Holmes, C. J., Evans, A. C. and Toga, A. W. (1997) Detection and mapping of abnormal brain structure with a probabilistic atlas of cortical surfaces. *J. Comput. Assis. Tomogr.*, in press.

Thurfjell, L., Bohm, C., Greitz, T. and Eriksson, L. (1993) Transformations and algorithms in a computerized brain atlas. *IEEE Trans. Nucl. Sci.*, 40, 1167–1191.

Toga, A. W., Ambach, K. L., Quinn, B., Hutchin, M. and Burton, J. S. (1994) Post mortem anatomy from cryosectioned human brain. *J. Neurosci. Methods*, 54, 239–252.

Toga, A. W., Thompson, P. M. and Payne, B. A. (1996) Modeling morphometric changes of the brain during development. In Thatcher, R. W., Lyon, G. R., Rumsey, J. and Krasnegor, N. (eds), *Developmental Neuroimaging: Mapping the Development of Brain and Behavior*, Academic Press, Orlando, FL.

Vaillant, M., Davatzikos, C. and Bryan, R. N. (1996) Finding 3D parametric representations of the deep cortical folds. *Proc. of the IEEE Workshop on Mathematical Methods in Biomedical Image Analysis*, pp. 151–159.

Van Essen, D. C. and Maunsell, J. H. R. (1980) Two-dimensional maps of the cerebral cortex. *J. Comparative Neurology*, 191, 255–281.